ADVANCED FUNCTIONAL MATERIALS
www.afm-journal.de

Materials Views
www.MaterialsViews.com

Polarization Dynamics in Ferroelectric Capacitors: Local Perspective on Emergent Collective Behavior and Memory Effects

*Rama K. Vasudevan, Daniel Marincel, Stephen Jesse, Yunseok Kim, Amit Kumar, Sergei V. Kalinin, and Susan Trolier-McKinstry**

Functional properties of ferroelectric materials depend both on the residual domain states and on the mobility of domain walls in response to the applied electric and stress fields. This paper reviews the use of multidimensional scanning probe microscopy to assess these factors in the time- and voltage domains, with an emphasis on the manner in which domain walls respond collectively to stimuli. It is found that in many $PbZr_{1-x}Ti_xO_3$-based capacitors, domain wall motion is correlated over length scales that exceed the domain and grain sizes by orders of magnitude, suggesting emergent collective electromechanical behavior. The role of mechanical boundary conditions and field history on the domain wall contributions and the stability of the ferroelectric domain state are discussed.

1. Ferroelectricity and Electromechanical Phenomena in Capacitor Structures

Ferroelectric materials possess a rich spectrum of pyroelectric, piezoelectric, and electro-optic properties, and are hysteretic in their response to applied electric fields. In addition, the dipolar polarizability typically produces large relative permittivities at frequencies in the microwave range and below. This rich variety of functional properties lends itself to use in a diverse array of applications, including thermal imaging devices; piezoelectric sensors, actuators, transducers; active optical components; holographic image storage; capacitors for charge storage; and nonvolatile memory elements.[1] The vast majority of these devices utilize components which are capacitive in character, e.g., the functional properties are accessed through electrodes which are usually large relative to the length scales associated with either the grain or the domain structure of the material.

Many of the field- and time-dependent responses of ferroelectric materials, including the dynamics of polarization reversal, nonlinear dielectric and piezoelectric responses, aging of the functional properties, and some of the frequency dependence of the permittivity,[2,3] are associated with motion (or the absence thereof) of domain walls in the material. There are a host of factors that can affect domain wall motion in ferroelectric materials, including grain boundaries, other ferroelectric or ferroelastic domain walls, phase boundaries, dislocations, point defects, some electrode/dielectric interfaces, and core-shell microstructures. One of the challenges that faces the field is the difficulty in isolating the role played by a single type of pinning center or domain wall in controlling the response of an electroded ferroelectric. Instead the amalgamated response of millions of domains and domain walls is probed.

On the macroscopic level, a variety of approaches for describing the collective materials response, including the contributions arising from extrinsic sources (e.g., domain wall and phase boundary motion) along with accompanying hysteresis have been reported. Of these, the Rayleigh law,[4–5] is one of the simplest formalisms. The Rayleigh law describes a linear increase in the dielectric and piezoelectric properties as a function of the ac field amplitude, providing the domain structure of the sample is unchanged by the driving field. The increase correlates directly with the observed hysteresis in the polarization or strain response, respectively. For the dielectric case, this is expressed by:[6,7]

$$\varepsilon' = \varepsilon_{init}' + \alpha' E_{ac} \tag{1}$$

$$P = \varepsilon_0(\varepsilon_{init}' + \alpha' E_{ac})\, E \pm \varepsilon_0 \frac{\alpha'}{2}(E_{ac}^2 - E^2) \tag{2}$$

where ε' is the dielectric permittivity, the applied field is $E = E_{ac}\sin(\omega t)$, t is time, ω is angular frequency, ε_{init}' is the reversible Rayleigh coefficient, α' is the irreversible Rayleigh

---

R. K. Vasudevan
School of Materials Science and Engineering
University of New South Wales
Kensington, 2052, Australia
Prof. S. Trolier-McKinstry, D. Marincel
Department of Materials Science and Engineering
Pennsylvania State University
University Park, PA 16802 USA
E-mail: STMcKinstry@psu.edu
Prof. S. V. Kalinin, Dr. A. Kumar, Dr. S. Jesse, Prof. Y. Kim[+]
The Center for Nanophase Materials Sciences
Oak Ridge National Laboratory
Oak Ridge, TN 37831 USA
E-mail: sergei2@ornl.gov
[+]Present address: School of Advanced Materials Science
and Engineering, Sungkyunkwan University, Suwon 440-746, South Korea

DOI: 10.1002/adfm.201203422

coefficient, P is the polarization, and ε_0 is the permittivity of free space. Here, $\varepsilon_{\text{init}}'$ includes contributions both from the intrinsic response and reversible motion of the interfaces, while α' quantifies irreversible motions of the interfaces. The intrinsic contributions arise from field-induced response of an ensemble of single domains.

Rayleigh behavior was first observed in magnetic materials.[8,9] There is an expanding literature that demonstrates that many ferroelectric samples behave as Rayleigh-like systems for field excursions up to ≈½ the coercive field, suggesting that Rayleigh-like behavior is common in ferroic systems.[7,10,11] Moreover, direct confirmation that Rayleigh behavior is associated with motion of non-180° domain walls has been reported for bulk ferroelectric ceramics.[12] The latter experiments also demonstrate that as domain walls move, the intrinsic response increases linearly with the amplitude of the ac electric field, presumably due to a reduction in the clamping of response by the adjacent material.

There are, however, a number of reasons why Rayleigh responses may not describe the hysteresis and nonlinearity, and other approaches, such as a Preisach-like model must be considered.[13] First, if the field excursions are large enough that the domain structure of the sample is perturbed during the measurement, then Rayleigh-like responses are not expected. Secondly, if the distribution of the restoring forces for the domain walls is not Gaussian, then curvature is introduced into the ac field dependence of the dielectric or piezoelectric constants.[14] However, the microscopic origins of Rayleigh and more complex dynamic behavior remain unexplored, hindering knowledge-driven optimization of materials properties and microstructure for advanced properties.

The last two decades have seen an explosion of research in ferroelectric films, both from the standpoint of implementing them into devices, and as a vehicle for probing the fundamental physics of complex phenomena in ferroic systems. Here again, the functional properties are assessed through electrodes in piezoelectric microelectromechanical systems, electrocaloric devices, pyroelectric detector arrays, and ferroelectric random access memory devices.[15,16] Moreover, given the fine domain structure observed in many thin films, electrical measurements typically probe many domains and/or grains, so that a collective response of the sample is observed.

Recent advances in scanning probe microscopy, near field optical microscopy, and in situ electron microscopy experiments have enabled the dynamic responses of ferroelectric materials to be probed locally. These measurements are providing new insight into the way in which domain walls move, pin, and contribute to both the materials response and its hysteresis. This paper reviews both the methodology employed in piezoresponse force microscopy, and its application to probing the local and mesoscopic responses of ferroelectric materials. A short description of the techniques that will be described in the paper is given in **Table 1**. Thin films are used as model systems both to assess measurement methodologies, and as a means of gaining new insights regarding the contribution of domain walls to piezoelectric response, thus contributing to understanding of emergent electromechanical phenomena in these systems.

Stephen Jesse is a research staff member at Oak Ridge National Laboratory in the Imaging Functionality group at the Center for Nanophase Materials Sciences. He develops novel scanning probe microscopy (SPM) techniques to facilitate functional nanometer-scale imaging and dramatically increase the amount of information gathered. This includes coupling voltage, radio-frequency, and photonic excitation and detection systems to extend SPM to the fundamental time and energy scales characteristic of photovoltaic, mechanical, electromechanical, and electrochemical processes. He develops methodologies to analyze and interpret high-dimensional, multi-spectral datasets. Stephen received his PhD (2004) from the University of Tennessee, Knoxville in Materials Science and Engineering.

Yunseok Kim is an assistant professor of School of Advanced Materials Science and Engineering at Sungkyunkwan University (SKKU). He received his PhD degree from Korea Advanced Institute of Science and Technology (KAIST) in 2007. From 2008 to 2010, he was awarded the Humboldt research fellowship from the Alexander von Humboldt foundation which allowed him to work as a postdoctoral researcher at Max Planck Institute of Microstructure Physics, Halle, Germany. Then, he worked as a postdoctoral researcher at Oak Ridge National Laboratory from 2011 to 2012. His research interests include scanning probe microscopy studies of nanometer-scale electromechanical, transport, ferroelectric, and ionic phenomena.

Susan Trolier-McKinstry is a professor of ceramic science and engineering, director of the W. M. Keck Smart Materials Integration Laboratory and co-director of the Nanofabrication facility at the Pennsylvania State University. Her main research interests include understanding the mechanisms that control structure- processing-property relationships in dielectric and piezoelectric thin films, developing new electromechanical measurement capabilities, and utilizing thin films in microelectromechanical systems. She is a fellow of the American Ceramic Society, an academician of the World Academy of Ceramics, a fellow of IEEE, and a member of the Materials Research Society.

Table 1. Band-Excitation SPM Techniques. x and y are the spatial coordinates for mapping, ω is the angular frequency. BE denotes the band excitation method.

Name* (Abbreviation)	Variables	Applications
Piezoresponse force microscopy (BE-PFM)	$x \times y \times \omega$	Basic imaging of electromechanical (domain structures) and conservative/dissipative mechanical properties
Switching-spectroscopy piezoresponse force microscopy (BEPS)	$x \times y \times \omega \times$ voltage	Local switching behavior, hysteresis loop mapping
AC spectroscopy	$x \times y \times \omega \times$ AC voltage	Piezoelectric nonlinearity. The magnitude of AC bias is altered in this technique.
First order reversal curves (FORC)	$x \times y \times \omega \times$ voltage × voltage	History-dependent studies. Similar to a sequence of hysteresis loops, with larger excitation windows at each step.
Dynamic piezoresponse force microscopy (D-PFM)	$x \times y \times \omega \times$ voltage × time	Relaxation studies. Similar to BEPS, except the piezoresponse is measured over time after each pulse to probe relaxation behavior.
Switching dynamic spectroscopy piezoresponse force microscopy (SDS-PFM)	$x \times y \times \omega \times$ voltage × time	Domain dynamics (nucleation and growth) as a function of pulse amplitude and pulse width.
Nonlinear harmonic mapping	$x \times y \times \omega \times$ AC voltage × harmonic	Nonlinear contributions to the electromechanical response

*Note that all of the techniques listed employ the band-excitation method for signal generation and detection; however, some (e.g., switching spectroscopy PFM, or SSPFM, and relaxation studies) were originally implemented in the single-frequency mode.

2. Principles of Piezoresponse Force Microscopy

2.1. Principles of PFM: Single Frequency and Band-Excitation

Piezoresponse force microscopy (PFM)[17] has emerged as an indispensable technique for non-destructive probing and mapping domains in piezo/ferroelectric nanoparticles, thin films, nanotubes, and nanomesas.[18–21] Recently, PFM has been expanded to include a suite of voltage- and time-based spectroscopies,[22–25] which allow thermodynamic and kinetic aspects of polarization switching to be probed at the nanometer-scale, while providing the ability to spatially correlate these phenomena with microstructural features of the sample.

The basic PFM setup consists of an atomic force microscope (AFM) with a conductive tip on the end of a reflective cantilever in contact with the sample. In a classical single-frequency PFM, a lock-in amplifier generates a sinusoidal wave of a set (reference) frequency and voltage, which is sent to the tip. The piezoelectric sample expands or contracts due to the local piezoelectric response, causing the tip and cantilever to deflect. Both vertical and lateral (i.e., torsional) deflections of the cantilever are measured by a beam deflection (laser/photodiode) setup in the AFM.[26] The local strain, which depends on the local remanent polarization, P_r, underneath the tip, is then measured via the amplitude and phase of the deflection signal at the reference frequency. Concurrently, the local topography can also be captured from the dc (low frequency) component of tip deflection. For coarse domain structures, scanning across the sample produces a map of the ferroelectric domains that are present in the sample (with some convolution with flexure modes when large top electrodes are employed). In this way, the PFM images of vertical and/or lateral domains in the sample can be acquired simultaneously with the surface topography.

Single frequency PFM is generally carried out at low frequencies and is relatively straightforward for materials which have large converse piezoelectric coefficients d_{ijk} (or d_{im} in matrix notation). A typical scanning probe microscope can detect deflections as small as ≈5 pm (response close to resonance; 50–200 pm away from the resonance), whereas a prototypical ferroelectric system, such as Pb(Zr, Ti)O_3 (PZT) thin-film will have a $d_{33,f}$[27] on the order of 10–100 pm/V,[28] suggesting that the deflections due to the field-induced strain can easily be detected with a 1V_{PP} sine wave applied to the tip. However, many materials (e.g., biological systems, III-V nitrides, thin ferroelectric films) exhibit much weaker electromechanical coupling coefficients in the range 1–10 pm/V.[29–31] In such instances the applied sinusoidal bias must be 1–10V_{PP}, which can be large enough to cause breakdown of the sample, electrochemical surface damage, or polarization switching.[32]

Improved sensitivity can be achieved by measuring the system's response at the contact resonance frequency of the cantilever, thereby increasing the signal to noise by the quality factor of the cantilever, Q. Additionally, by measuring at these higher frequencies, more spectroscopic information can be acquired for the same measurement time. At low frequencies, the cantilever's transfer function is relatively flat (Q≈1),[33] but at the first contact resonance, the quality factor can be as high as ≈50–200 for a stiff cantilever in contact with the surface. However, a problem is immediately apparent: the peak width of the contact resonance is sharp, on the order of ≈2–5 kHz, but the cantilever resonance fluctuates (by ≈ tens of kHz even for relatively flat surfaces) due to variations in the tip-surface contact area across the sample. This necessitates an approach to track the resonant frequency of the cantilever.[34] In classical SPM methods utilizing piezoelectric driving, this problem has usually been circumvented by use of a phase-lock-loop system wherein the driving frequency of the oscillator is altered to maintain a constant phase for the response signal. However, such an approach fails for PFM, as the phase of the response changes due to the presence of ferroelectric domains, and other approaches need to be found.

One solution to this problem is *band-excitation*, wherein the response is captured across a band of frequencies around the cantilever resonance.[35] A band of frequencies is sent to the tip,

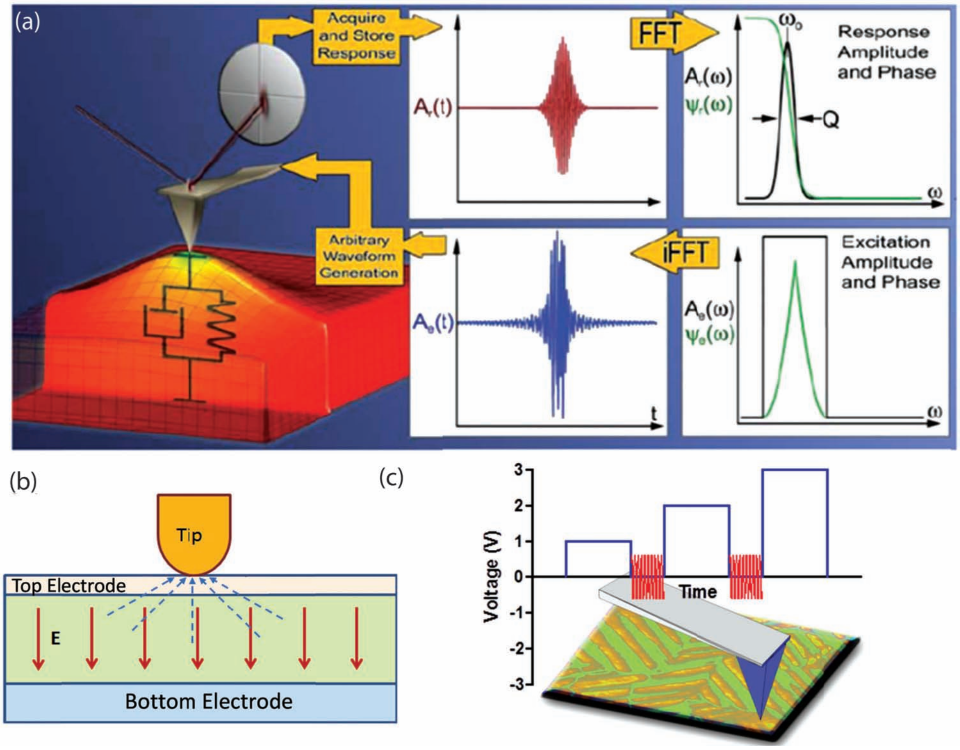

Figure 1. BE-PFM and PFM spectroscopies. a) Schematic of band-excitation PFM. An arbitrary waveform generator is used to generate an excitation signal across a band of frequencies, which is then sent to the tip. The response is monitored over time, and, after FFT, the response over the frequency space is recovered. Reprinted with permission.[35] Copyright 2007, IOP Publishing Ltd. b) Geometry and field-distribution for the top-electrode PFM setup. The field is macroscopically uniform (neglecting fringing effects at the edge of the capacitor), and independent of tip position. The detected strain field is indicated by the dashed blue lines, which converge at the tip. c) In voltage and time-based spectroscopies, the tip is held at a fixed position on the sample and voltage pulses (blue) are applied to the tip. The response is then detected through a high-frequency read signal (red).

and the response is measured over time and fast Fourier transformed (FFT) to retrieve the frequency-dependent response of the system. The basic principles of this approach are illustrated in **Figure 1**a. By fitting the frequency dependent response to a simple harmonic oscillator (SHO) function, the system's response parameters, namely amplitude, resonance, quality factor and phase can be captured,[34] allowing the electromechanical (amplitude), conservative (resonant frequency) and dissipative (Q-factor) mechanical properties of the sample to be separated as parallel information channels. The improvements in sensitivity also allow piezoelectric properties to be assessed at lower electric fields.

2.2. Image Formation in Capacitors

PFM can be performed on structures in air, vacuum, or liquid[36] at different temperatures[37] and for materials with and without top electrodes.[38] For tip-electrode PFM, both the electric field established in the material and the strain response are highly localized, allowing for high-resolution imaging. In the case where a top-electrode is present, as in ferroelectric capacitor geometries (see Figure 1b), the applied field is uniform and the excitation is global regardless of the position of the SPM tip. However, care must be taken as the signal interpretation is more complicated than in the case without a top-electrode. Though the surface displacement as measured by the tip is local, it arises from a convolution of the local surface deformation and the collective piezoresponse of the area underneath the electrode (possibly including flexure of the substrate), since the whole electrode area is excited. In this way, PFM in the capacitor geometry allows collective interactions to be probed.

The image formation mechanism for PFM using a capacitor geometry has been reported elsewhere.[39] Briefly, the effect of using a top electrode is to average the signal across the material's thickness.[40] For thin capacitors, the *measured* domain wall width scales with the thickness of the ferroelectric layer and the top electrode thickness. For most ferroelectric materials, where the top electrode is much thinner than the film thickness, the lateral resolution can be estimated as ≈0.2H, where H is the thickness of the ferroelectric layer.[39] For granular films or systems with poor mechanical connectivity between the grains, the resolution can be significantly higher as can be readily analyzed based on the strain distribution on the system induced by uniform external field.[39,41]

2.3. Basic Voltage and Time-Based PFM Spectroscopy

In addition to imaging domain structures, a biased PFM tip can be used to manipulate the local polarization state (local ferroelectric switching). This approach can be extended to study both thermodynamic and kinetic phenomena through voltage and time-based spectroscopic methods in PFM.[25] The basic idea is shown in Figure 1c, i.e., the tip is placed on the sample at a particular point, and a DC voltage waveform is applied (blue). The response can then be measured either in the on-field state, or the off-field state, through detection of response to high-frequency probing signal (shown in red). By repeating the measurement for different applied voltages, it becomes possible to construct the system's response to the applied field, producing the electromechanical hysteresis loop. Similarly, the technique can be applied to pulse trains, i.e., where the DC voltage pulse amplitude is kept constant, but the pulse width (or magnitude) is altered, to monitor domain nucleation and growth. Such a setup is known as 'stroboscopic' PFM[22] and allows imaging of the polarization switching process.

Alternatively, the response of the system over time can be monitored to determine the degree of domain relaxation. Such methods can highlight the role of defects on relaxation process, including the reversal of in-plane *a*-domains mediated by switching of adjacent 180° *c*-domains,[42] or the competition between elasticity and disorder in determining the velocity of domain wall motion.[43]

Pioneering work on PFM imaging of domain structures in capacitor geometries was carried out by Gruverman et al.[22,44] In these studies, a pulse train was employed, with PFM imaging between the pulses, to determine the domain dynamics in IrO_2/PZT/Pt capacitors. An initial set pulse to pole the capacitor was followed by a write pulse of fixed amplitude. PFM was then performed after the write pulse and the process was repeated for different pulse widths. Assuming that the polarization reversal always follows the same path, the quasi-static measurement performed after each write pulse allows visualization of the dynamics of the polarization reversal process. The authors extracted the switched domain fraction from the PFM images and fit the polarization reversal curve to the Kolmogorov–Avrami–Ishibashi (KAI) model,[45,46] finding that while the model worked well for the nucleation-dominated stages of the switching process, it failed to describe the later (slower) stage of the switching process. Instead, the nucleation-limited switching model[47] (NLS) provided a much better fit to the experimental data in this region. These PFM based capacitor studies of domain dynamics shed light on the differences in polarization reversal in microscopic geometries, which can depart substantially from traditional macroscopic theories.

Domain dynamics during polarization reversal in $SrRuO_3$/Pb(Zr, Ti)O_3/$SrRuO_3$ capacitors by PFM were also explored in a series of studies by Noh et al.[43,48–51] The nucleation centers were studied by applying a write pulse of fixed amplitude, imaging, then resetting the capacitor and repeating the experiment. In this way, a spatial nucleation probability map was constructed. It was found that nucleation generally began at the same sites in the capacitor, providing support for the assumption that domain reversal will follow the same pathway on multiple switching cycles (return point memory). Moreover, the number of nucleation sites was shown to increase linearly with the logarithm of the switching time. It is also intriguing that the nucleation sites for positive and negative bias were different, suggesting that electrode/ferroelectric interface influences the nucleation.

The same group studied the nonlinear dynamics of domain wall propagation in PZT capacitors over a wide range of temperatures.[43] Through analysis of PFM images in conjunction with switching currents, the domain wall velocity as a function of the applied field and temperature was obtained. Analysis of the curves revealed that at 300 K, at low fields (≈0–0.2 E_c) domain walls were pinned, leading to creep-type behavior,[52] whereas intermediate fields (>≈0.2 E_c) resulted in depinning of the domain walls and a nonlinear increase in velocity with the applied field. At fields well above E_c, the wall velocity was increased further, and was mostly independent of temperature. The studies also highlighted the random-field nature of disorder in PZT capacitors, as well as the fractal nature of the domain walls.[53]

3. SSPFM and BEPS

3.1. Collective Effects and Clustering in SSPFM

The ability to correlate local measurements of electromechanical response with sample microstructure is a key advantage of voltage-based PFM spectroscopies. Of these, switching-spectroscopy PFM (SSPFM) (single frequency excitation)[54] and band excitation switching spectroscopy PFM (BEPS),[55] based on acquisition of multiple hysteresis loops on a dense spatial grid of points, provides an avenue to explore the local variations in polarization switching behavior of ferroelectric materials. Numerous SSPFM/BEPS studies have been reported on the interaction of pinning centers, such as grain boundaries,[56,57] pre-existing domain walls[58–60] and surface defects[61] on domain nucleation and growth.

In SSPFM and BEPS, the local hysteretic response is mapped as a function of position. A DC stepped triangular waveform (i.e., a series of rectangular pulses with a triangular waveform envelope) is then applied to the tip, and the response of the system is measured through band-excitation PFM. In BEPS, fitting the BE response data to a simple harmonic oscillator allows the piezoresponse to be extracted and plotted as a function of the applied bias, yielding the local hysteresis loop. In SSPFM, the piezoresponse is measured directly as a first harmonic of the tip response to driving bias. Analysis of the hysteresis loops yields the key characteristics of the local switching behavior, e.g., the imprint, coercive fields, the work of switching (defined as the area under the loop), and the remanent polarization. These parameters can then be mapped as 2D images to assess spatial variation of switching behavior on either free or electrode surfaces.

Here, SSPFM is illustrated for polycrystalline $PbZr_{0.52}Ti_{0.48}O_3$ thin films (1.09-μm thick, ≈50-nm lateral grain size, deposited on Pt-coated Si substrates via chemical solution, with a 50-nm-thick Pt top electrode).[62] SSPFM mapping (50 by 50 pixels over the same 6 μm × 6 μm region) was undertaken for excitation field windows below and above the coercive field. Piezoresponse data were acquired at zero dc bias, after the sample had been exposed to higher bias (e.g., in the "off-state", to obtain remanent loops), to avoid complications associated with the dc field dependence of the $d_{33,f}$ piezoelectric constants and electrostatic contributions

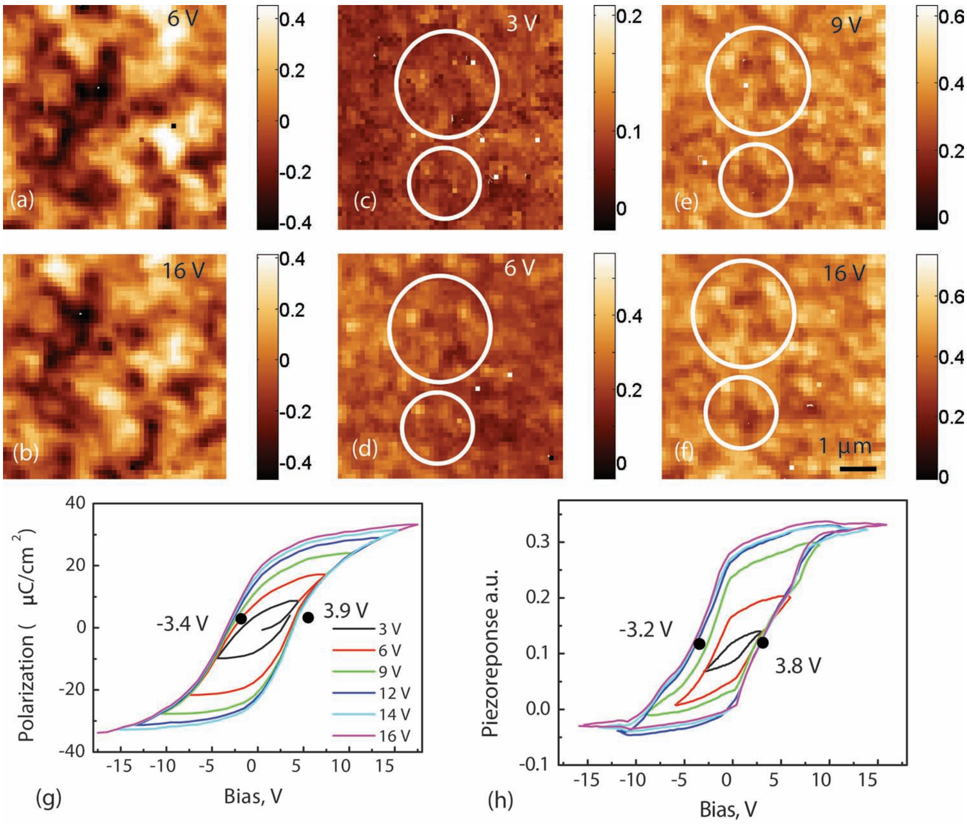

Figure 2. SSPFM of PZT capacitors. a–f) Evolution of the hysteresis loop as a function of the applied bias voltage. a,b) show the remanent piezoresponse maps. c–f) are switchable response maps with increasing excitation windows (units: PFM amplitude (a.u)). g) Minor and major hysteresis loops calculated from the irreversible part of the Preisach density, assuming the sample was depoled prior to the field excitation. h) Averaged local SSPFM loops for similar excitation windows. Figure reprinted with permission.[62] Copyright 2009, American Physical Society.

to the signal.[63] The measured switchable response is then a function of changes in the domain state within the signal generation volume of the probe. This approach thus allows probing domain dynamics below the resolution of the PFM.

The spatial distributions of the remanent and switchable piezoresponses are shown in **Figure 2**a–f. The remanent piezoresponse images remain similar after multiple switching cycles, suggesting that at the end of the switching cycle each pixel returns to the initial mesoscopic state (return point memory).[64] At the same time, the switchable response map shows a gradual evolution with increasing voltage excitation. For the lowest excitation fields, the switchable response (measured at zero field after field exposure) is zero. As the excitation field increases, the average switchable response increases, as expected for progressive opening of the hysteresis loop. The local hysteresis loops (representing the response of ≈100–300 nm diameter regions) vary spatially, and differ significantly from the macroscopic response. However, the macroscopic response can be reproduced when the local loops are averaged over the scan area (neglecting a constant offset due to the macroscopic bending of the wafer as a piezoelectric bimorph). A comparison of the P-E loops (shown in Figure 2g) calculated from Preisach distributions determined on large capacitors (≥200 µm diameter) and averaged PFM loops from 6 µm × 6 µm areas in Figure 2h illustrate that saturation for both occurs at ≈ 12–16 V. Similarly, a comparison of the coercive biases defined with respect to the horizontal symmetry axis (i.e., $P = 0$ for P–E and piezoresponse = 0.15 for PFM) yields coercive biases of –3.2 and 3.8 V for PFM data and –3.4 and 3.9 V for the P-E data. This suggests that the observed Preisach behavior for macroscopic capacitors originates at length scales *above* the ≈100-nm resolution limit of PFM, but below the image size. Furthermore, this illustrates the contribution of macroscopic bending modes to the PFM signal, inevitable for macroscopic bimorph- and unimorph type structures.

This spatially-correlated behavior is further illustrated in the correlation functions for the 2D SSPFM maps. **Figure 3**a shows that the average feature size in the switchable response maps is ≈200–500 nm. These significantly exceed the average feature size in the topographic images, thus excluding the possibility of topographic cross-talk. Correlations at length scales exceeding ≈1 µm are also evident in the switchable response image (Figure 3b). To explore this behavior further, shown in Figure 3c is the loop correlation function $RV(L)$, defined as,

$$RV(L) = \sum\nolimits_V \sum\nolimits_{i\,j\in L} \left[PR^+(V) - \left\langle PR^+(V)\right\rangle L\right]^2 \tag{3}$$

where PR^+ is the voltage dependence of the (positive branch) of the piezoresponse signal, while PR^- corresponds to the negative branch. The function $RV(L)$ indicates these ≈1.5 µm features

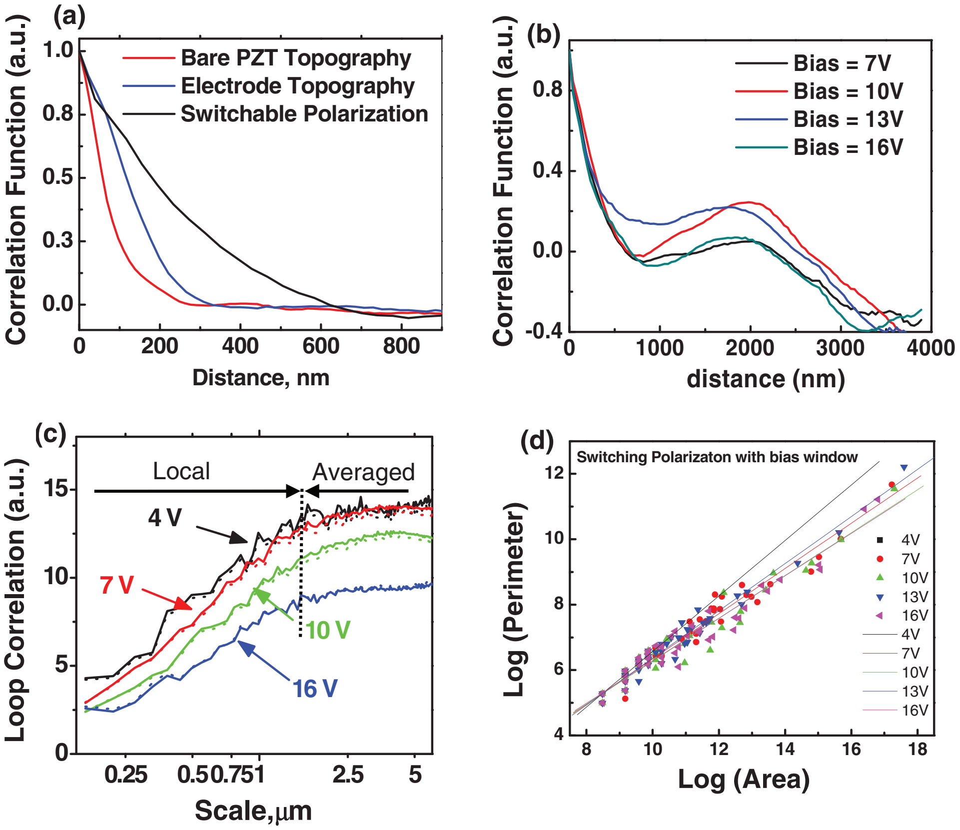

Figure 3. Correlation analysis for PZT capacitors. a) Comparison of the correlation widths from the switchable response images with the electrode and bare PZT topography images. b) Spatial autocorrelation functions at different bias voltages. c) RV(L) (Loop correlations) for different excitation windows. d) Fractal analysis, computed by analyzing the switchable polarization maps for different excitation windows. Reprinted figure with permission.[62] Copyright 2009, American Physical Society.

persist for excitation bias levels from 7–16 V and likely represent the collective response of regions with ≈10^2–10^3 grains. Additionally, fractal analysis of the area was undertaken, using the switchable polarization images for different excitation windows, with the results plotted in Figure 3d.

It is worth emphasizing that though displacement measured by the SPM technique is local, it arises from a convolution of the local surface deformation and the collective piezoresponse of the entire sample underneath the electrode, since the whole volume is excited. Moreover, because the electric field is uniform in the sample, the measured response is influenced by the existence of neighbouring nucleation or pinning sites. Correlated motion of domain walls would then be responsible for the observed clustering in the response. Therefore, this, and all of the techniques discussed in this paper probe collective interactions, while at the same time showing the local spatial variation in the measured parameters.

4. Piezoelectric Nonlinearity: Reversible and Irreversible Motion of Domain Walls

It is also interesting to assess whether or not spatial correlation of domain wall motion occurs when measurements are made well *below* the sample coercive field (e.g., in the Rayleigh regime). Rayleigh measurements can be performed via BE-PFM when the amplitude and phase of the surface deflection is measured as a function of the amplitude of the excitation voltage. The measured response amplitude, $A_{\max}$ is related to the excitation voltage V_{ac}, as $A_{\max} = a_1 + a_2 V_{\mathrm{ac}} + a_3 V^2_{\mathrm{ac}}$, where the amplitude is proportional to the surface displacement h, such that $A_{\max} = \beta h$. Here, β describes the transfer function of the cantilever. Differentiating with respect to V_{ac} and converting to electric field, E_{ac}, yields the Rayleigh law $\beta d_{33,f} = \beta d_{33,init} + \beta\alpha_d E_{\mathrm{ac}}$ where $\beta d_{33,\text{ init}} = a_2$ and $\beta\alpha_d = 2a_3 t$ and film thickness is t. The local nonlinearity is then $2a_3t/a_2 = \alpha_{\mathrm{d}}/d_{33,\mathrm{init}}$. Notably, this parameter is independent of the cantilever properties,[65] and hence can be measured quantitatively.

Nonlinearity measurements following the Rayleigh law quantify the motion of domain walls at subcoercive fields, rather than domain nucleation. Measurements are made on poled and aged samples in order to achieve a strong response under small drive fields. Because the response under a well-defined electric field is essential for comparison to macroscopic measurements, a capacitor structure with the signal applied between top and bottom electrodes is employed, using the PFM tip as a sensor to measure vertical displacement.

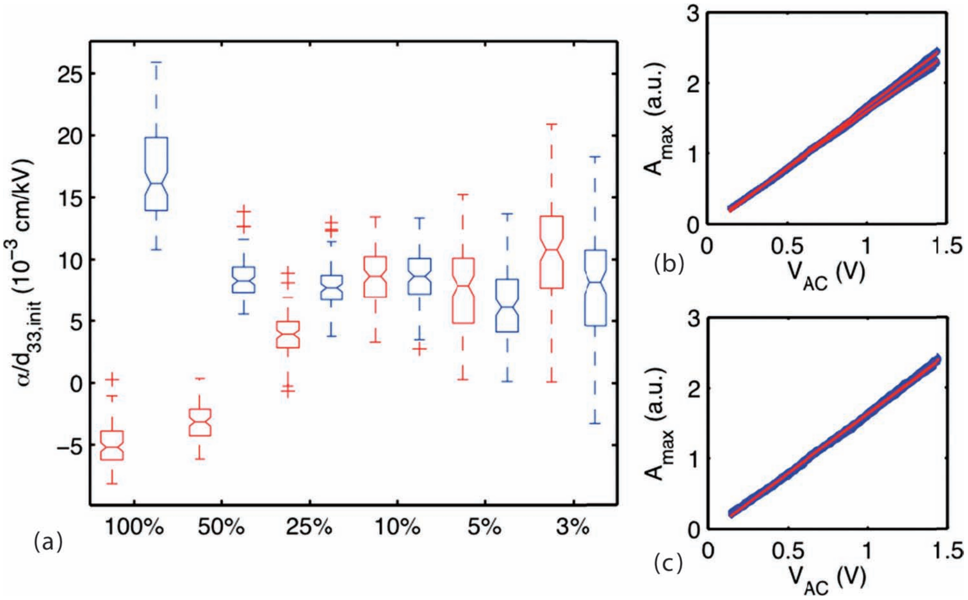

Figure 4. Tip surface nonlinearity. Piezoelectric nonlinearity measurements on a PZT film with top and bottom electrodes. a) Box plot of the distribution of nonlinearity as a function of percent chirp character of the excitation signal, with the increasing frequency sweep in red and the decreasing frequency sweep in blue. Signals with high chirp character show large tip surface nonlinearities, while signals with high sinc character show low signal to noise ratio. b,c) Amplitude of the response as a function of excitation voltage for signals with b) 50% and c) 10% chirp character. The response of each of the 100 measurements is shown in blue with the average linear response for chirp up and chirp down in red. Differences in the red lines indicate tip surface nonlinearities.

4.1. Mechanical Nonlinearities in the Tip Surface Junction

Although the intent of PFM studies is to characterize the nonlinear *material response* as a means of probing domain wall motion, the measured nonlinearity is a combination of both the material response and cantilever dynamics. Hysteresis in the resonance frequency of the cantilever tip in contact with the sample surface with increasing voltage and sweep direction is characteristic of nonlinearities arising from the cantilever dynamics. It was found in BE-PFM measurements that dynamic nonlinearities suppress the maximum amplitude for increasing frequency with time, or chirp up, and amplify the maximum amplitude and decrease the resonant frequency for decreasing frequency with time, or chirp down, as indicated in **Figure 4**a–c.[66]

In order to measure the material nonlinear response, the nonlinearity due to cantilever dynamics, and hysteresis in the resonance frequency with sweep direction, must be minimized. The nonlinearity due to the cantilever dynamics is a function of the energy of the excitation signal. Therefore, it is possible to minimize the nonlinearity by minimizing the energy of the excitation signal. This can be achieved by using a pure sinc function (i.e., well-localized in time) for the excitation. However, the signal to noise ratio decreases with increasing sinc character and increases with an increasing chirp character, so a balance must be found where sufficient signal to noise is achieved while minimizing the tip nonlinearities.

It has further been shown that when BE-PFM measurements are made on a capacitor structure, the optimal energy of the excitation signal is constant across a single electrode and does not depend on the position on the electrode. Because the necessary excitation signal will not vary between regions in the test area, it follows that the measured nonlinearity due to the piezoelectric response of the material is quantitative and local.

4.2. Domain Wall Motion in Ferroelectric Capacitors at Subcoercive Fields

The local nonlinear piezoelectric response was first observed via PFM by Bintachitt et al.[65] in $PbZr_{0.52}Ti_{0.48}O_3$ (PZT) ferroelectric films clamped on a Pt-coated Si substrate. In this study, micron-sized regions with high nonlinear response were observed in a matrix of lower nonlinear response (see **Figure 5**). This observation of local nonlinearity proves that small volumes of ferroelectric material exhibit Rayleigh behavior. The clusters of high nonlinear response were attributed to local regions of less strongly pinned domain walls than in the matrix. It is intriguing that the cluster size significantly exceeded either the grain or domain size in those films (similar to the SSPFM studies), as will be discussed below.

Variation in the clusters of nonlinear response was observed with a change in thickness of the films, as shown in Figure 5b. Films thicker than 2 μm showed uniform nonlinearity. This was attributed to the measured response averaging over a larger sample volume such that individual clusters could not be identified. It was estimated that the density of regions of high nonlinear response for these polycrystalline PZT films was on the order of 1 per μm^3 such that the response appears homogeneous when the resolution is above 1 μm^3, as was the case for the thicker films.[15] In thinner films, clusters of high nonlinear response were observed in a matrix of low nonlinear response,

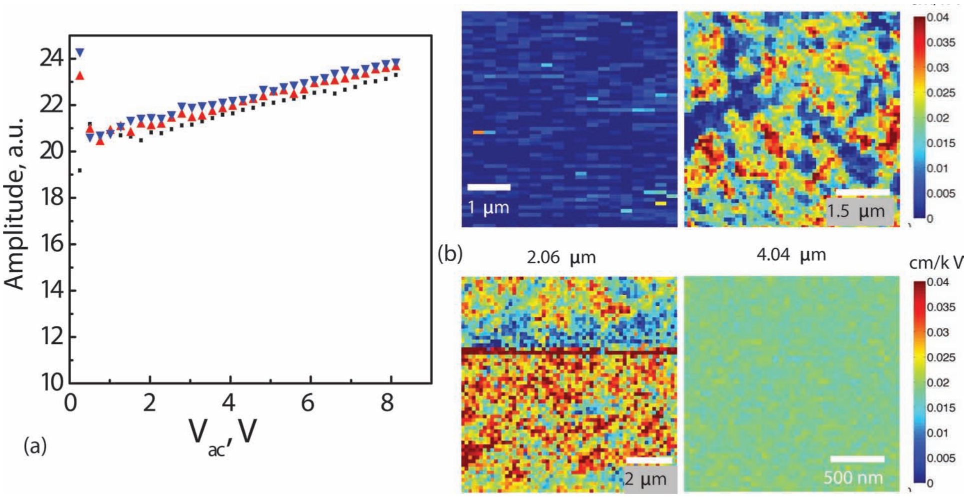

Figure 5. Piezoelectric nonlinearity in polycrystalline PZT films with top and bottom electrodes. a) Field dependence of $d_{33,f}$ in a 4-µm-thick sample, b) maps of the piezoelectric nonlinearity in PZT films of different thickness. Adapted and reproduced with permission.[65] Copyright 2010, National Academy of Sciences.

with the density of high response regions decreasing with film thickness. Finally, in the thinnest film the electromechnical nonlinearity was uniform and essentially zero. This evolution agreed with the observation of a decreasing global dielectric nonlinearity with decreasing thickness below 1–2 µm.[67]

The observed regions of high nonlinearity were interpreted as the cascading movement of domain walls[68] due to the motion of one wall imposing an effective pressure on walls within an interaction volume. Furthermore, the cluster size observed was much larger than the grain size of the material,[65] leading to the interpretation that there is a strong correlation of domain wall movement between grains. It is intriguing that the observed clustering of high nonlinear response in the 1.09 µm thick sample in Figure 3 (on the order of ≈0.5–2 µm laterally) is comparable to the regions of correlated switching in higher field measurements on similar films.[69] These two findings suggest that there is a correlation between regions of high nonlinear response and regions of correlated switching, indicating a similar mechanism is responsible for both, namely the simultaneous displacement of interacting domain walls across regions with reduced pinning.

One of the key points made in the initial paper on nonlinearity measurements by Bintachitt et al.[65] is a similarity between the global dielectric nonlinearity and the local piezoelectric nonlinearity measurements. However, in other experiments,[70,71] the local piezoelectric nonlinearity was much reduced relative to the global dielectric nonlinearity for clamped films. It is noteworthy that the sample analyzed by Bintachitt et al.[65] was randomly oriented and finer-grained while the samples analyzed by Griggio et al.[70,71] were textured. The difference in dielectric and piezoelectric nonlinearities was attributed to a difference in the population of domain walls which contributes to the irreversible component of the dielectric and piezoelectric properties. In addition, regions with negative nonlinearity observed in the textured samples, which were attributed to hard local behavior, also decrease the average piezoelectric nonlinearity.

4.3. Role of Mechanical Boundary Conditions

Because ferroelectric materials undergo a spontaneous strain upon polarization, they are typically ferroelastic as well. As such, it is not surprising that the observed domain state and domain wall mobilities in ferroelectric films depend on the mechanical boundary conditions experienced by the sample. Numerous observations have been reported on increases in response associated with more mobile domain structures on laterally relieving the clamping associated with the substrate.[72,73]

Mechanical clamping can also be reduced by changing the sample geometry from a film to a nanotube. Bharadwaja et al.[74] and Bernal et al.[21] both reported fabrication of PZT-based nanotubes using Si and soft templates respectively. The former group demonstrated that the ratio of the irreversible to the reversible dielectric Rayleigh constants was larger for the nanotube than for a thin film of the same thickness. Comparable results were obtained by Bernal et al. using PFM to probe the response along the length of the nanotube wall.

Recently, the influence of reduction in substrate clamping on the lateral extent of correlated domain wall motion was also reported using released diaphragm structures.[71] The sample studied was an oriented PZT morphotropic phase boundary film, released by an isotropic XeF_2 dry-etch step in a circular pattern under the electrode. Local BE-PFM measurements were taken on the clamped region, the released region, and the interfacial region on the same capacitor structure. As in other measurements on clamped regions, strong clustering of regions of high nonlinear response was observed in the clamped region on this sample. However, the nonlinear response was substantially more uniform in the released regions (particularly well away from the clamped boundary), as shown in **Figure 6**. Indeed, the spatial average of $\alpha_d/d_{33,init}$ increased from 0.005 ± 0.015 cm kV^{-1} in the clamped region to 0.013 ± 0.003 cm kV^{-1} in the released region with a much tighter distribution of nonlinearity in the released region.

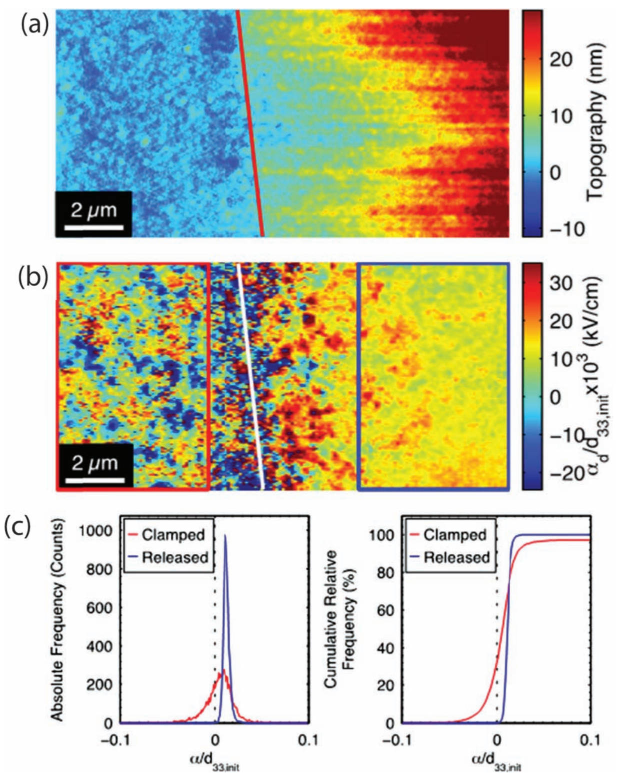

Figure 6. The role of clamping on nonlinear response. a) Released diaphragm structure topography. The red line shows the edge of the released region: to the left of the line, the film is clamped to the underlying Si substrate; right of the line, the sample is released by undercutting the Si. b) Nonlinear response, $\alpha_d/d_{33,init}$; the white line shows the edge of the released region, the bounding red and blue boxes are the regions used for histograms. c) Absolute frequency and cumulative frequency histograms of clamped and released regions, showing narrower distribution and higher average nonlinear response in the released region relative to clamped region. These data are similar to those from Griggio et al.,[71] but arise from a separate measurement.

Dielectric measurements were also acquired for fully clamped structures, released structures, and released and broken structures. The released structures had reduced local stresses at the film-substrate interface, while the released and broken regions also experienced a change in the average tensile stress in the film (due to differences in the thermal expansion of the film and substrate). Significant increases in dielectric nonlinearity were observed for the broken diaphragm structures.

The increase in the local piezoelectric nonlinear response on undercutting the substrate was attributed to a greater mobility of domain walls, which was further corroborated by frequency dispersion measurements of the global dielectric nonlinearity.[71] For the clamped capacitors, α_e exhibited greater frequency dependence than the released capacitors, indicating that a greater portion of the irreversible domain wall motion freezes out at higher frequencies. Also, ε_{init} for the clamped capacitors exhibited a lesser frequency dependence than the released capacitors, indicating a greater contribution from reversible domain wall motion.

The narrower distribution of nonlinear response for the released region and the loss of clustering were attributed to an increase in the length scale for correlated motion of domain walls. Taking into account a greater number of domain walls moving irreversibly with a greater length scale for correlated movement, it is clear that clamping at the ferroelectric-substrate interface provides strong pinning sites. The pinning was attributed to a combination of a partial release of the average tensile stress due to the difference in thermal expansion of the film and substrate and also a release of local stresses due to the substrate rigidity. During domain formation, deformation strains can couple mechanically with the substrate rigidity, producing a local stress at the ferroelectric-substrate interface, which can be expected to influence domain wall mobility. Therefore, reduction of these local stresses may remove strong pinning sources and lead to a much greater correlated movement of domain walls over an increased length scale. Further strengthening the above observations, it was found that the global dielectric irreversible coefficient of the released and broken capacitor was 27.2 ± 0.07 cm kV^{-1}, approaching values similar to undoped morphotropic phase boundary ceramics.[71]

5. Dynamic Piezoresponse Force Microscopy: Time-Resolved Probing of Polarization Dynamics

In the previous sections, it was shown that PFM and voltage spectroscopy modes provide powerful tools to probe polarization switching spatially, and can facilitate study of the history-dependent responses of such systems. Typically, it is presumed that the hysteresis loops are determined by thermodynamics of the switching process, and are independent of the bias sweep rates. However, it has been widely demonstrated from macroscopic measurements of dielectric and piezoelectric properties, as well as SPM studies of domain dynamics in single crystals and relaxor ferroelectrics, that the ferroelectric domain state can change on a time scale of milliseconds to days.[75,76] The driving force behind such aging can be stabilization of the normal ferroelectric domain structure in response to local electric or elastic fields[43,77,78] or polarization instabilities in relaxors,[79] or factors such as slow surface charge dynamics or ionic motion.[80,81] An approach to systematically probe kinetic effects locally during voltage spectroscopy using dynamic switching spectroscopy PFM (D-PFM) is discussed in this section.

In D-PFM, the pulse sequence is the same as in SSPFM/BEPS. However, the electromechanical response is measured as a function of time after the pulse, providing information on aging on the millisecond time scale with spatial resolution. The size of the full 5-dimensional data set ($x \times y \times$ voltage steps $\times$ time steps $\times$ frequency bins) is typically ≈1–10 GB (depending on number of sampling points and parallel information channels, e.g., vertical or vertical and lateral) and acquisition time is 2–10 h. As an example of the technique, the D-PFM method has been applied to quantify polarization relaxation in polycrystalline ferroelectric capacitors.[82]

The D-PFM response at a single point is illustrated in **Figure 7**a,b; relaxation is apparent in the PFM signal on both the positive and negative voltage sweeps. Because the measurement is performed on a capacitor structure, electrochemical processes[32] can largely be excluded, and the observed relaxation can be attributed to polarization dynamics.

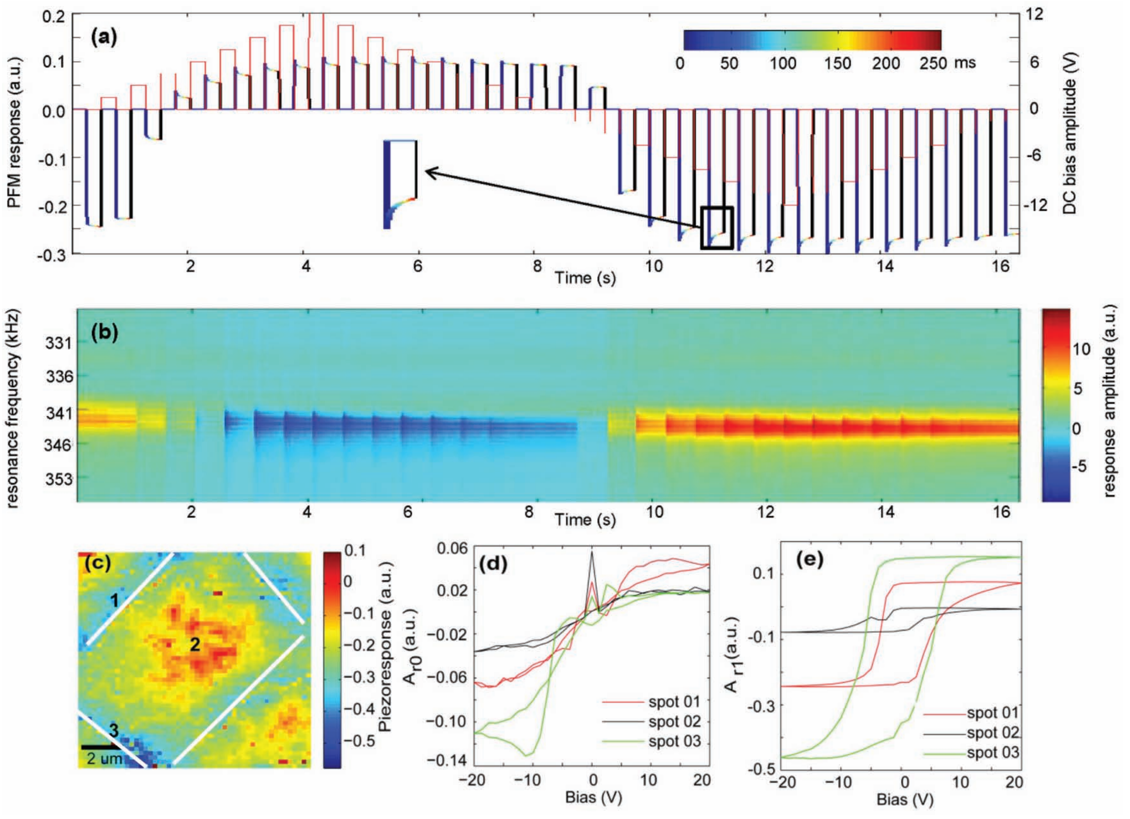

Figure 7. Dynamic PFM. a) Piezoresponse at a single location obtained on a PZT ferroelectric capacitor using D-PFM. Signal relaxation is observed after each bias pulse (with more relaxation for larger changes in bias). The response is overlaid on the bias scheme for visualization of the relaxation hysteresis. The color scheme shows the evolution of response after each voltage pulse in time domain. b) Frequency-amplitude spectrogram for relaxation hysteresis at a single location shows clear relaxation of the piezoresponse amplitude with time after each pulse (in the off state). c) Piezoresponse map across a PZT capacitor with microcrack-like features on the capacitor surface at 2 V_{ac}. These crack-like features are indicated by the white solid lines. Plots of relaxation fit parameters d) A_{r0} (V) and e) A_{r1} (V) vs. applied bias for three different locations as shown in (c) are plotted in three different colors. The data for A_{r0} (V) has been multiplied by 3 for spot 1 and spot 2 for better visualization. The spatial variation in the relaxation behavior is evident. Reproduced with permission.[82] Copyright 2012, American Institute of Physics.

The piezoresponse map for the capacitor is shown in Figure 7c. The map reveals cracks in the PZT layer that developed after prolonged cycling at high fields. The larger response amplitudes immediately adjacent to the crack likely stem from release of clamping as discussed in Section 4.3. At the same time, there is no evidence of delamination of the ferroelectric film or electrode. The relaxation data were analyzed using exponential fitting function $A_r(t) = A_{r0} + A_{r1}\exp(-t/\tau_d)$ where A_{r0} is the offset, A_{r1} is the relaxing magnitude, and τ_d is the relaxation time, and is shown in Figure 7d, e. In all locations selected from the map in Figure 7c, the offset component shows pronounced hysteresis with an "ideal" loop shape. However, the hysteresis loops are all shifted significantly in the vertical direction.

The relaxation times are relatively noisier than the other two parameters. The relaxation times are largest at zero bias and decrease linearly with different slopes for positive and negative voltages, meaning that the relaxation is slowest when the domain state is not strongly perturbed by the previous pulse. The relaxing part shows almost complete lack of hysteresis. The voltage dependence of the relaxation amplitude follows an S-shape for most points studied, i.e., it is linear at small positive and negative bias, and saturates for larger fields. Interestingly, the saturation tends to occur well above the nucleation and coercive biases of the sample. This is consistent with the observation that the piezoelectric coefficients tend to be both larger and more stable with prolonged exposure (often > 10 min) to poling fields. The ability to map the relaxation response may ultimately provide clues as to what factors produce some of the slower polarization dynamics in ferroelectric films.

The D-PFM approach can be applied to ferroelectric materials and devices, and can also be extended to ionic systems.[80,83–87] We note that the combination of spatially resolved hysteresis and relaxation data is of particular interest in exploring the statistical physics of other ferroic systems such as disordered ferromagnetic materials.

6. Emergent Approaches for Probing Polarization Dynamics

6.1. Switching Dynamic Spectroscopy PFM (SDS-PFM)

Most measurements of nanometer-scale switching dynamics in ferroelectric capacitors provide spatially correlated information

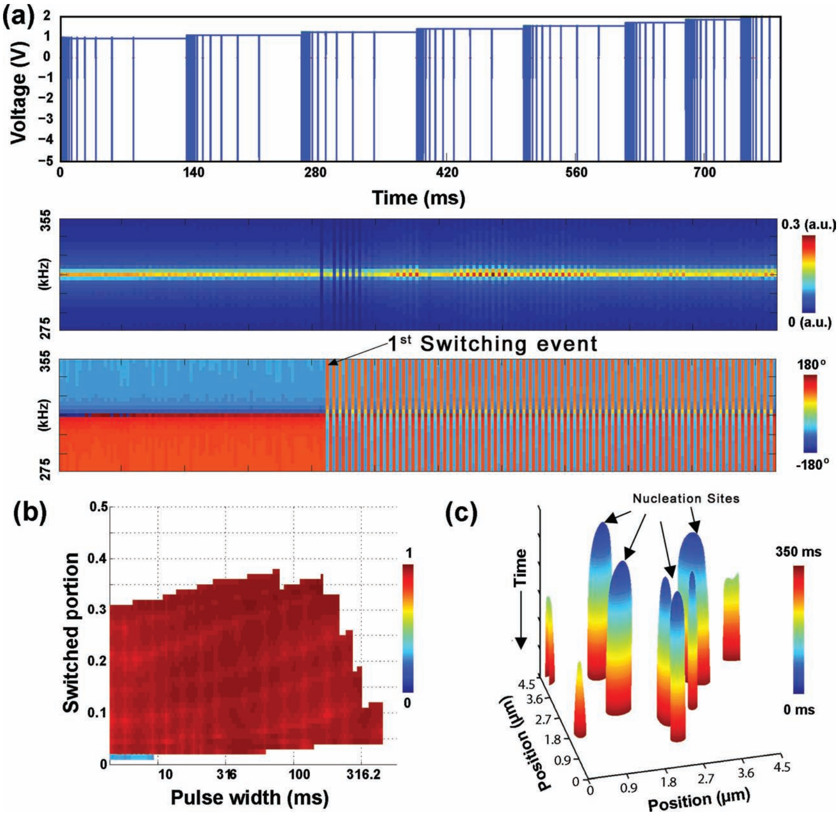

Figure 8. Switching dynamic spectroscopy PFM (SDS-PFM). a) (top) Switching waveform of each point for SDS-PFM measurements and corresponding BE amplitude (middle) and phase (bottom) spectra at a single point. b) Correlation as a function of pulse width over the entire measured area. c) Position of domain wall for 670-nm-thick epitaxial rhombohedral (001)-oriented $Pb(Zr_{0.52}Ti_{0.48})O_3$ capacitors under +1.4 V. Scale bar is 1 μm. The color bar indicates the pulse width.

on the switching dynamics over a limited range of parameters only. An emerging approach to provide a more extensive data set is switching dynamic spectroscopy PFM (SDS-PFM), which collects a 5D data set $P(x, y, V, t, \omega)$. To explore the V, t dependent switching dynamics over an x-y space using SDS-PFM approach, the switching waveform of **Figure** 8a(top) is applied at each grid point, and the response is measured using the BE approach. As an example, SDS-PFM was performed on a (001)-oriented 670-nm-thick epitaxial $Pb(Zr_{0.52}, Ti_{0.48})O_3$ film with top-electrodes, deposited on $SrRuO_3/SrTiO_3$. A 4.4 ms set pulse of a –5 V, was applied for the background poling. Then pulse amplitudes from +0.95 V to 2.00 V, (near the coercive voltage of the film) were applied for various pulse widths. At each pulse step and each spatial location, switching information was monitored by application of the band excitation (BE) waveform.[35] As a result, BE amplitude and phase spectra can be obtained at each spatial location, as shown in Figure 8a (middle and bottom). The phase spectrum clearly shows when the first local switching event occurs, and is indicated in the figure. Furthermore, it can be seen in the amplitude spectrum that the amplitude of the piezoresponse is dependent on the magnitude and width of applying bias pulse. This is expected, since the piezoresponse is proportional to the fraction of domains switched, with higher fractions switched for larger bias amplitudes and pulse widths.

SDS-PFM can provide information on the microscopic domain configurations during switching process as well as multi-dimensional domain growth behavior. Figure 8b shows correlation as a function of pulse width over an area of 4.5 μm × 4.5 μm. The correlation parameter of ‘1’ (‘0’) in Figure 8b represents that domain configurations are identical (uncorrelated). Since all of the values in Figure 8b are close to unity, the correlation map for the dependence of the switched fraction on pulse width shows that the V, t parameter space is nearly independent of the degree of switching. This indicates that nucleation and subsequent domain growth generally follow the same pattern independently of exact field history.

Because of this universality of switching pathway, the level set method (LSM)[88] can be applied for the analysis of SDS-PFM data as shown in Figure 8b. LSM is a numerical technique for tracking interfaces and shapes and, so can be used to assess domain wall motion inside the ferroelectric capacitor throughout the switching process. Figure 8c shows the position of domain walls, indicating where and when in the field cycle nucleation occurs, and how domains grow from the nucleation sites. The preferential nucleation sites, which can be identified as blue colored peaks, gradually grow laterally, as shown by the cone-like structures. It also appears that after nucleation at several sites, the velocity of domain growth abruptly slows, because the width of the cone-like structures does not increase significantly with larger pulse widths. This approach can further be used to quantify the velocity and directional dependence[89] of domain wall motion. Thus, SDS-PFM is expected to be a powerful tool for exploring domain wall dynamics over a wide parameter space in high spatial and temporal detail.

6.2. First Order Reversal Curve Mapping

Ferroelectrics, like other hysteretic systems, show strong field-history dependence of local properties. As a result, knowledge of the hysteresis response for one field history generally does not guarantee prediction of the response to a different history, a consideration of significant importance for applications ranging from sensor and actuators to computer memories and data storage. Remarkably, this behavior can be both an obstacle for applications (e.g., hysteresis in actuators) and enable new device concepts (e.g., neuromorphic memories).[90–92]

Preisach[93] and Mayergoyz[13] demonstrated that, provided the material response to applied fields satisfies conditions of wipe-out and congruency, the response of a hysteretic system for an arbitrary field history can be treated using a collection of bistable units (hysterons) having statistically distributed coercive and bias fields. Each unit is characterized by a rectangular hysteresis loop and its status is determined by the actual field and history of the applied external fields. The distribution of these hysterons can be determined from the first-order reversal curve measurements (FORC) and allows the response for arbitrary field history to be reconstructed.

To get insight into local mechanisms underlying Preisach behavior, Néel[94] and Kronmuller[95] analyzed the reversible and irreversible single domain wall dynamics in a defect-induced potential energy profile, thus explaining Preisach behavior as a result of the dynamic response of a single domain wall. In contrast, macroscopic models have also been put forward[96,97] suggesting that nonlinearity arises from domain wall depinning, manifesting as a field-power law for the dielectric or piezoelectric coefficient. Determining the origins of Preisach behavior, therefore, requires nanometer-scale FORC measurements.

As an example, we present a nanometer-scale FORC study of a cracked ferroelectric capacitor using BE-PFM. In a cracked film, the mechanical constraints associated with clamping the film to the substrate are relieved near the crack. As a result, the material in that region can respond to applied electric fields more easily. The typical FORC BE-SSPFM bias envelope is shown in the lower part of **Figure 9**a. The setup and configuration remain similar to those used in BE-SSPFM, except that the bias envelope replicates a first order reversal curve. The frequency-amplitude spectral response is shown above the bias waveform in Figure 9a. The piezoresponse map of the studied region is shown in Figure 9b, and selected loops from the studied region are shown in Figure 9c, which reveals clear variation in overall switching behavior (outer loop) as well as the FORC behavior. This data was further analyzed by using principal component analysis[98,99] (PCA). PCA is a statistical technique that decomposes a dataset into a set of eigenvectors (termed 'principal components') and associated eigenvalues (termed 'loadings'). The selection of the eigenvectors is such that the first eigenvector accounts for the largest possible variation in the dataset, the second also accounts for the highest variation with the constraint that it be orthogonal to the first, and so on, until all the variation in the dataset is captured. The spatial variability of the FORC behavior can be seen in the loading maps from the first three components from PCA of the FORC loops, shown in Figure 9d–f. The corresponding Preisach densities computed from these three principal components is shown in Figure 9g–i. These studies can help determine the mechanisms behind macroscopic theories of hysteresis, and test the length scales over which they may be applicable.[100]

6.3. Nonlinear Harmonic Mapping

In the prior sections, techniques for measurement of material response as a function of voltage, time, voltage cycling and spatial position were presented. It was shown that at small fields, domain wall motion produces nonlinearity in the functional properties of strongly piezoelectric PZT films.[57,77–81] Nonlinearity can also arise from electrostriction,[101] and the effect of inter-granular coupling on the intrinsic piezoelectric response.[12,102] In some cases, these contributions can be separated. One commonly used technique is to examine the system's higher harmonic response[103] to the field: phenomena such as Joule heating[104,105] and electrostriction,[106] for instance, produce second-order harmonics to the response, whereas the strictly linear couplings do not. Thus, via exploration of the response space of higher harmonics, such mechanisms can be decoupled.

Most studies on higher harmonic responses have been reported for bulk samples, where only averaged responses can be probed. In principal, a general n^{th} harmonic SPM-based detection method can provide local information on higher harmonic responses, using the band-excitation method. To investigate the response at the n^{th} order harmonic, a band of frequencies around ω_0/n, where ω_0 is the first cantilever resonance first excited, as shown in **Figure 10**a. The response is then measured around ω_0 and Fourier transformed to return the system's response in frequency space. In this way, the amplification of the signal by the cantilever's quality factor is still exploited, greatly improving the signal-to-noise while still probing only the nonlinear interaction.

An example of this technique, for first and second harmonics, is shown in Figure 10b,c, where the 1st and 2nd harmonic response of a 600-nm-thick tetragonal, epitaxial $PbZr_{0.45}Ti_{0.55}O_3$ thin film at the same location is plotted for increasing probing bias V_{ac}. This is then repeated across a grid of points to yield the spatial variation in the response. The utility of this technique is confirmed by the spatial maps for the first and second harmonics at 2 V_{ac}, which are shown in Figure 10d,e. These maps show different areas of response, highlighting that the origins of the signals differ. The average piezoresponse amplitude as a function of V_{ac} across the sample (≈2500 points) is shown in Figure 10f, with quadratic fits to the data graphed as solid curves. It is easily seen that the responses differ for the two harmonics, due to the different origins of the measured signal. Therefore, this natural extension of PFM should provide significantly more ability to delineate multiple contributions to the electromechanical response signal.

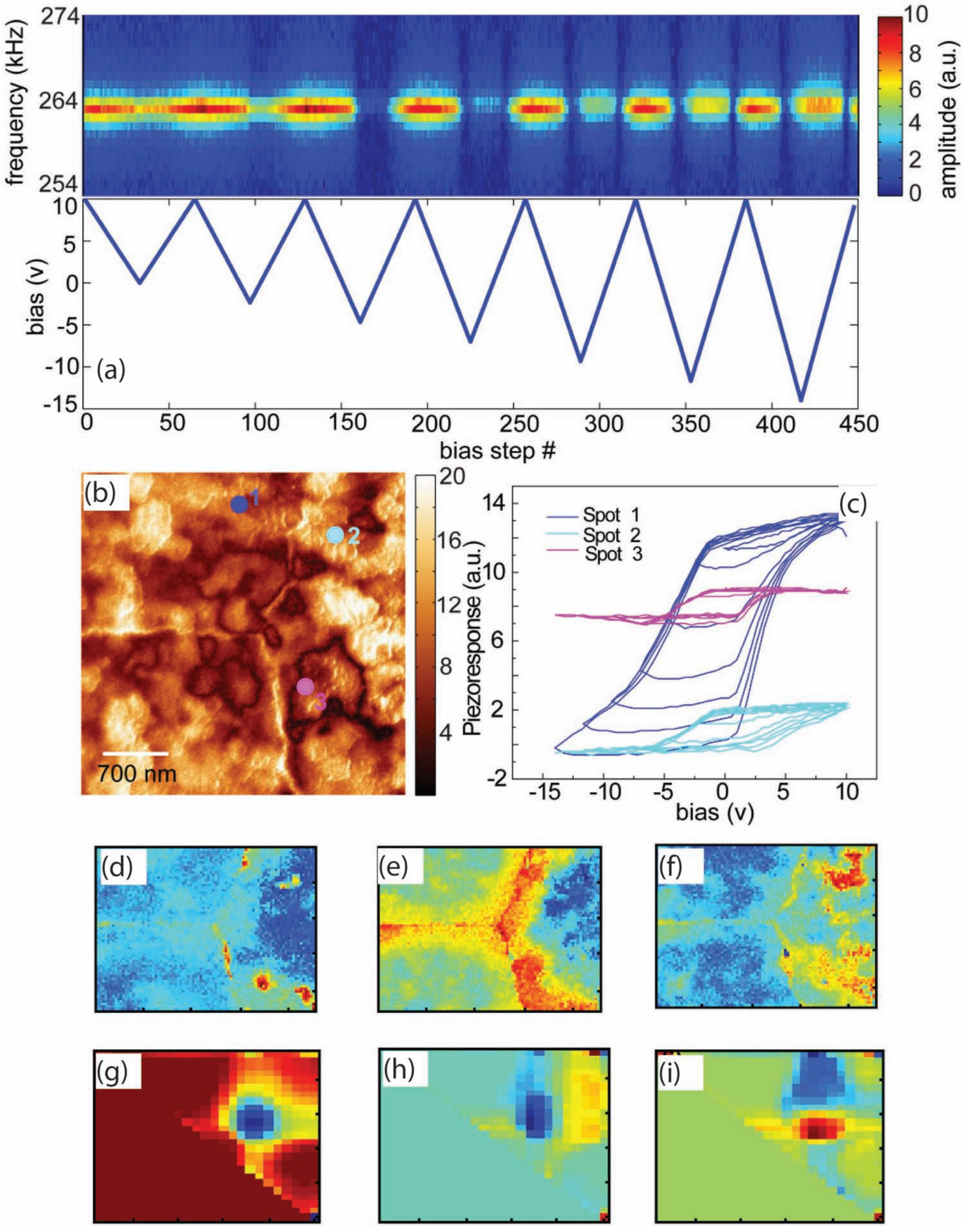

Figure 9. FORC studies in cracked PZT capacitors. a) Frequency-amplitude spectrogram at different bias steps using FORC waveform obtained from a PZT ferroelectric capacitor. b) piezoresponse map across a PZT capacitor with microcrack-like features on the capacitor surface using 1 V_{ac}. c) selected FORC loops from three points on the map in (b). d–f) Spatial variability of the FORC behavior shown in loading maps from the first three PCA components of the FORC loops. g–i) The Preisach density maps obtained from first three principal components from the PCA of local FORC loops.

Harmonic mapping in ferroelectrics could prove useful in exploring domain wall motion, particularly as the technique evolves to allow measurements at lower fields. For example, in the original Rayleigh model, the macroscopic nonlinear piezoelectric response caused by irreversible domain wall motion leads directly to the formulation of odd higher-order harmonics.[4] By building on this model to include the reversible motion of any interface, Bassiri–Gharb et al.[106–108] showed in a 'dynamic poling' model that reversible (or nearly reversible) wall motion can produce a second-order harmonic response to the piezoelectric strain. Nonlinear harmonic mapping therefore provides an avenue to investigate, locally, the contributions of reversible and irreversible domain wall motion, and probe energy loss spatially.

6.4. Interpretation of PFM Spectroscopies

The application of single-frequency and BE based switching spectroscopy PFM approach to the capacitor structures yields high-density 3D data sets of hysteresis loops at each location on the sample surface. However, while for tip-electrode

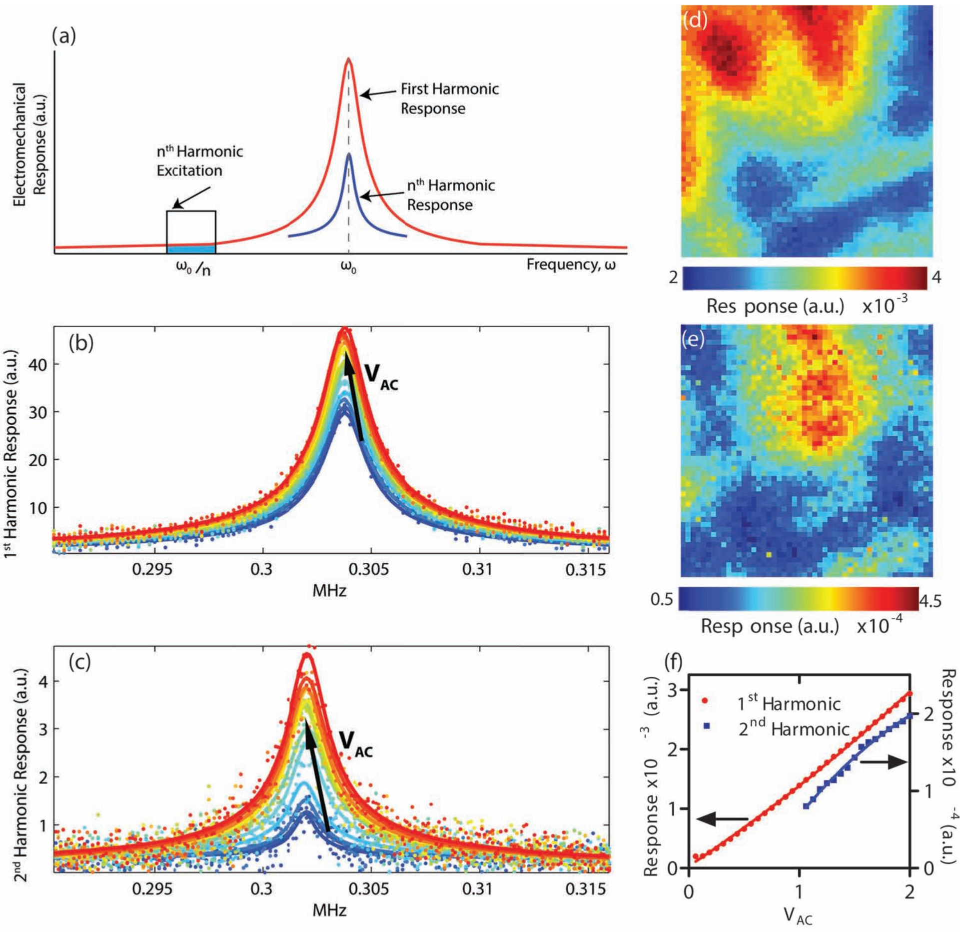

Figure 10. Nonlinear harmonic mapping. a) Illustration of the basic principle of resonance-enhanced harmonic detection. b) First harmonic and c) second harmonic electromechanical response at a single point, as a function of probing field V_{ac}. The raw data across the frequency spectrum is plotted as dots, with the solid lines the simple harmonic oscillator fits to the data. Spatial maps of d) first and e) second harmonic amplitude measured at V = 2 V_{AC}, measured across a 1 μm × 1 μm region of a PZT ferroelectric capacitor clearly show different response. The mean response for both harmonics across the studied region as a function of V_{AC} is plotted in (f).

PFM the switching is local, thus allowing for deterministic theory,[108–112] in the capacitor case switching is generally non-local. The measured hysteresis loop thus represents the convolution of polarization dynamics in the (macroscopically) uniform field and local detection, necessitating development of numerical pathways for analysis. One such approach can be based on classical phenomenological models such as Preisach density analysis; however, these models generally do not allow for mechanistic interpretation and variation of Preisach density across the sample surface does not allow for additional insight into local mechanisms. Approaches based on analytical function fits generally suffer from the lack of well-defined analytical models for hysteresis loop shape in ferroelectrics.

To circumvent this problem, we have suggested an approach based on the parametric fit of experimental data using results of multiple numerical experiments, referred to as *recognition analysis*.[114,115] As a prototypical model, we use the random bond-random field Ising model (as outlined for a magnetic material) defined as

$$H(H) = \sum_{i,j} J_{ij} S_i S_j + \sum_i (h_i + H) S_i \tag{4}$$

where $S_i = \pm 1$ are the local spins, J_{ij} are the nearest-neighbor interactions, h_i are the random fields, and H is the external field. The nearest neighbor interactions are assumed to have a Gaussian distribution with an average, J_0, and width, δJ, whereas the random field components have zero average and Gaussian distribution with width, δh. For specific parameter values this model reduces to classical physical behavior, e.g., ferromagnetic ($\delta h = 0$, $\delta J = 0$, $J_0 > 0$) or antiferromagentic ($\delta h = 0$, $\delta J = 0$, $J_0 < 0$) Ising model or Edwards-Anderson spin glass model ($\delta h = 0$, $J_0 = 0$). The dynamics of the system described by Equation (1) has been extensively studied.[115–117] The evolution of the system can be described by Glauber dynamics. Here, the spin flips if it is antiparallel to the local field $h^i_{loc} = \sum_j J_{ij} S_j - (H + h_i)$, i.e., for $h^i_{loc} S_i < 0$, and is stable for $h^i_{loc} S_i > 0$. The field follows triangular profile (including on and off state) similar to that used in experiments. The resulting hysteresis loop $S_H = \langle S_i(H) \rangle$ defines the field dependence of average magnetization as a function of model parameters, (J_0, δJ, δh).

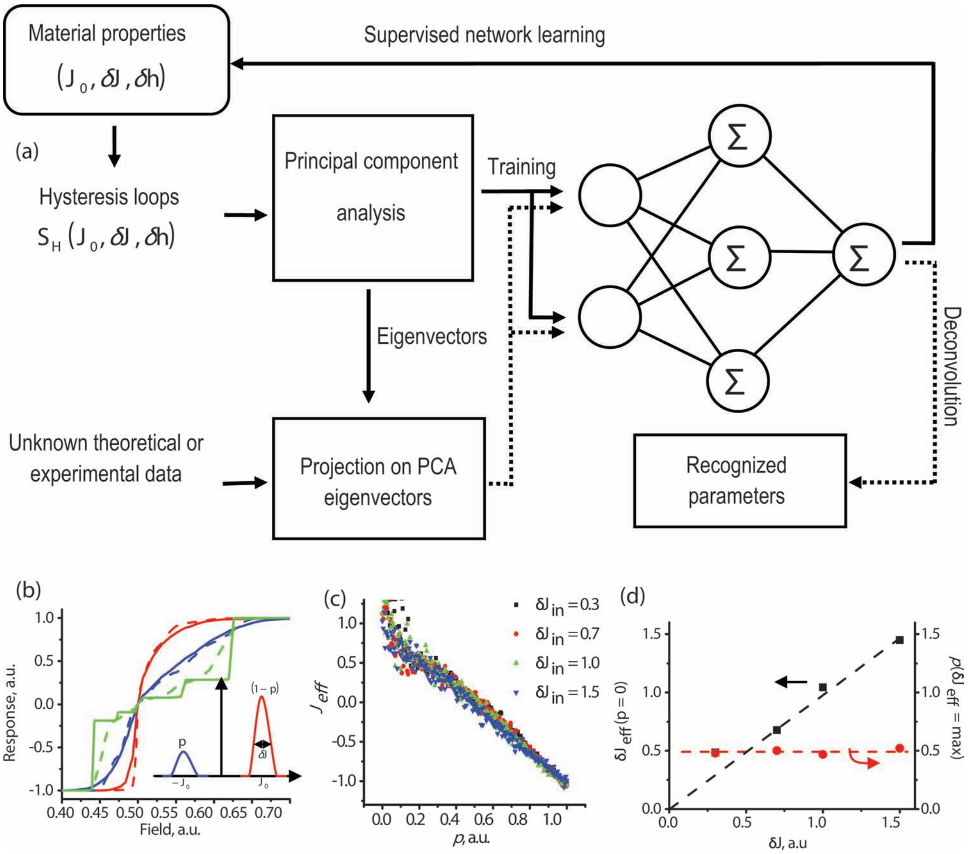

Figure 11. Neural networks. a) Schematics of neural network recognition analysis. b) Modeled (solid line) and reconstructed (dotted line) hysteresis loops for $\delta J = 0.3$ and $p = 0.2$ (red), 0.5 (blue), and 1 (green), with (inset) Distribution of exchange integrals in the *p*-model. c) Reconstructed exchange integral $J_{eff}(p)$ and d) reconstructed RB disorder $\delta J_{eff}(p)$ vs, flip probability, *p*. Reproduced with permission.[114] Copyright 2009, American Physical Society.

To extract the model parameters from the hysteresis curve, we utilize the non-parametric deconvolution method based on a combination of principal value decomposition with neural network interpolation[119,120] as shown in **Figure 11**a. The family of theoretical hysteresis loops $S_H(J_0, \delta J, \delta h)$ is generated using Equation (4) in the predefined region of parameter space.

Thus a generated family of hysteresis loops is de-correlated using PCA, i.e., they are represented as a superposition, $S_m(H_j) = a_{mk}w_k(H_j)$, of the orthonormal eigenvectors w_j universal for the data set with parameter-dependent loading coefficients $a_{mk} = a_k(J_0, \delta J, \delta h)$. The determined loading vector $a_k(J_0, \delta J, \delta h)$ is used to train a feed-forward neural network (NN) using the set of $a_k(J_0, \delta J, \delta h)$ as inputs and J_0, δJ, δh as desired outputs. A trained neural network acts as a universal interpolator that establishes a relationship between the hysteresis loop shape described through coefficients $a_k(J_0, \delta J, \delta h)$, and model parameters J_0, δJ, δh. On the recognition stage, the experimental or theoretical hysteresis loops $S_{\exp}(H)$ are projected on the same $w_k(H_j)$ to yield $\alpha_{i\_\exp}$ values. The latter are then fed into the neural net trained by theoretical curves to extract model-dependent J_0, δJ, δh. This recognition approach thus solves the inverse problem of Equation (4), i.e., identification of disorder strength from the hysteresis loop shape.

The utility of this approach is illustrated for *p*-model as shown in Figure 11b–d. In this model, the RF-RB Ising model is defined, and the random bonds are flipped from positive to negative value with probability, *p*. The results of the fitting for J_0 and δJ are shown in Figure 11b. The recognition fitting allows reconstruction of the hysteresis loops in the interval of *J* from strong ferromagnetic to antiferromagnetic through the spin-glass–state (except for $p = 1$, for which sharp jumps in response are observed). This indicates that the hysteretic behavior of the *p*-model is equivalent to an RB Ising model with Gaussian distribution of RB components with some effective exchange integral $J_{\text{eff}}(p)$ and distribution width $\delta J_{\text{eff}}(p)$. The effective exchange integral $J_{\text{eff}}(p)$ decreases linearly with the percent chance of flip almost independently of δJ as shown in Figure 11(c). As expected, $J_{\text{eff}} \approx J_0(1 - 2p)$. The $\delta J_{\text{eff}}(p)$ depends on flip probability, *p*, approximately parabolically, $\delta J_{\text{eff}} = a + b(p - p_0)^2$. The RB disorder is minimal and equal to the δJ_0 at the edges of the interval and maximal for $P_0 \approx 0.5$ (not shown).

The applicability of this approach is illustrated for a polycrystalline ferroelectric capacitor (e.g. the polarization analog of the above model). The recognition fit for the *J*-δJ-*h* family is shown in **Figure 12**a–c. For a selected area on the map as shown in Figure 12a, the average experimental and average of closest simulated loops are shown in Figure 12d,e. Notice that the "fit" (i.e., the calculated hysteresis loop for the model parameters determined from the neural net recognition) is similar to the target loop, despite the relatively high noise levels. Based on

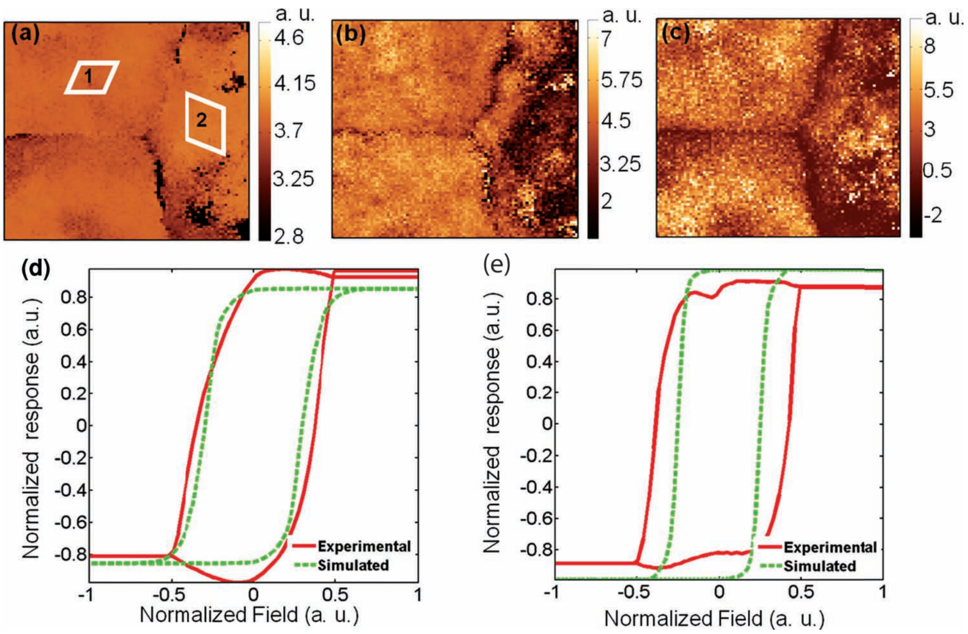

Figure 12. Reconstruction based on Ising model. Reconstructed maps for a) *J*, b) *δJ*, and c) *h* for the *J*- *δJ*-*h* family. d) Average experimental and average of closest simulated loops for the area 1 and (e) area 2 selected in map (a). Reproduced with permission.[113] Copyright 2011, American Physical Society.

this analysis above, we conclude that on the length scale of the spectroscopic measurements (0.3 µm $<L<$ 10 µm) the capacitor behaves as an almost spatially uniform RB-RF Ising system with strong ferroelectric coupling between the grains ($J_0 \approx \delta J$). The use of spectral imaging reveals the presence of mesoscopic (≈1 µm) fluctuations in disorder strengths, primarily attributed to the *J* and *δJ* terms. Specifically, the switching behavior are strongly affected in the vicinity of the crack due to partial strain release and loss of inter-grain coupling. Note that the decrease of both *J* and *δJ* observed in the reconstructed parameter maps for *J*-*δJ*-*h* families (Figure 11b,c) close to the crack over a length scale of ≈ grain size is in agreement with the chosen Ising-type model with near-neighbor interactions. In comparison, larger-scale contrast seen in the field disorder component is consistent with the strain-induced variations of electromechanical fields on the length scale of the film thickness.

7. Perspectives

Ferroelectric capacitors offer a rich model system for studying emergent electromechanical and dielectric responses. However, theoretical exploration of these systems has often been hindered by the extreme complexity of the problem, necessitating averaged phenomenological descriptions and precluding development of detailed mechanistic models.

Despite being at an early stage, locally resolved studies have allowed significant insight into nucleation and domain wall dynamics in capacitor structures. In addition, in complex polycrystalline systems, a set of unexpected behavior such as large-scale clustering of nonlinear responses, and significant role of the mechanical constraints were discovered. These spatially resolved techniques further necessitate development of multivariate statistical and physics-based models for visualization interpretation of (readily available) multidimensional data sets in terms of material-relevant parameters.

While demonstrated here for polycrystalline ferroelectric films, these techniques can be further adapted for relaxor ferroelectrics and other multiferroic systems with strong electromechanical coupling. Furthermore, the existence of electromechanical coupling in ionic and electrochemically active solids, ranging from energy storage and conversion materials and electroresistive electronics,[87,121–126] suggests the tremendous potential of these probes to explore fundamental nanometer-scale mechanisms operational in these materials and devices.

Acknowledgements

The authors acknowledge V. Nagarajan (University of New South Wales) for collaborations and multiple discussions. R.K.V. acknowledges the ARC Discovery Project Scheme and the user facilities at ORNL-CNMS under user proposal No. 2011–281. S.T.M. gratefully acknowledges the National Science Foundation and the National Security Science and Engineering Faculty Fellowship. S.V.K., S.J., Y.K., and A.K. acknowledge support from the Scientific User Facilities Division, DOE BES. The multidimensional PFM modes are available as a part of user program at the Center for Nanophase Materials Sciences (CNMS), www.cnms.ornl.gov.

Received: November 21, 2012
Revised: January 3, 2013

---

[1] A. J. Moulson, J. M. Herbert, *Electroceramics: Materials, Properties, Applications*, John Wiley and Sons Ltd., Chichester **2003**.
[2] M. P. McNeal, S.-J. Jang, R. E. Newnham, *J. Appl. Phys.* **1998**, *83*, 3288.
[3] L. Jin, V. Porokhonskyy, D. Damjanovic, *Appl. Phys. Lett.* **2010**, *96*, 242902.
[4] L. Rayleigh, *Philos. Mag.* **1887**, *23*, 225.

[5] D. V. Taylor, D. Damjanovic, *J. Appl. Phys.* **1997**, *82*, 1973.
[6] D. Damjanovic, *J. Appl. Phys.* **1997**, *82*, 1788.
[7] D. A. Hall, *J. Mater. Sci.* **2001**, *36*, 4575.
[8] T. Nattermann, Y. Shapir, I. Vilfan, *Phys. Rev. B* **1990**, *42*, 8577.
[9] L. Dante, G. Durin, A. Magni, S. Zapperi, *Phys. Rev. B* **2002**, *65*, 144441.
[10] O. Boser, *J. Appl. Phys.* **1987**, *62*, 1344.
[11] N. Bassiri-Gharb, I. Fujii, E. Hong, S. Trolier-McKinstry, D. Taylor, D. Damjanovic, *J. Electroceram.* **2007**, *19*, 49.
[12] A. Pramanick, D. Damjanovic, J. E. Daniels, J. C. Nino, J. L. Jones, *J. Am. Ceram. Soc.* **2011**, *94*, 293.
[13] I. D. Mayergoyz, *Phys. Rev. Lett.* **1986**, *56*, 1518.
[14] D. A. Ochoa, J. E. García, I. Tamayo, V. Gomis, D. Damjanovic, R. Perez, *J. Am. Ceram. Soc.* **2012**, *95*, 1656.
[15] N. Setter, D. Damjanovic, L. Eng, G. Fox, S. Gevorgian, S. Hong, A. Kingon, H. Kohlstedt, N. Y. Park, G. B. Stephenson, I. Stolitchnov, A. K. Taganstev, D. V. Taylor, T. Yamada, S. Streiffer, *J. Appl. Phys.* **2006**, *100*, 051606.
[16] S. Trolier-McKinstry, P. Muralt, *J. Electroceram.* **2004**, *12*, 7.
[17] M. Abplanalp, L. M. Eng, P. Günter, *Appl. Phys. A: Mater. Sci. Process.* **1998**, *66*, S231.
[18] F. Johann, T. Jungk, S. Lisinski, A. Hoffmann, L. Ratke, E. Soergel, *Appl. Phys. Lett.* **2009**, *95*, 202901.
[19] B. J. Rodriguez, S. Jesse, J. Kim, S. Ducharme, S. V. Kalinin, *Appl. Phys. Lett.* **2008**, *92*, 232903.
[20] C. S. Ganpule, V. Nagarajan, B. K. Hill, A. L. Roytburd, E. D. Williams, R. Ramesh, S. P. Alpay, A. Roelofs, R. Waser, L. M. Eng, *J. Appl. Phys.* **2002**, *91*, 1477.
[21] A. Bernal, A. Tselev, S. Kalinin, N. Bassiri-Gharb, *Adv. Mater.* **2012**, *24*, 1160.
[22] A. Gruverman, B. J. Rodriguez, C. Dehoff, J. D. Waldrep, A. I. Kingon, R. J. Nemanich, J. S. Cross, *Appl. Phys. Lett.* **2005**, *87*, 082902.
[23] A. Gruverman, D. Wu, H. J. Fan, I. Vrejoiu, M. Alexe, R. J. Harrison, J. F. Scott, *J. Phys.: Condens. Matt.* **2008**, *20*, 342201.
[24] A. Kumar, O. S. Ovchinnikov, H. Funakubo, S. Jesse, S. V. Kalinin, *Appl. Phys. Lett.* **2011**, *98*, 202903.
[25] R. K. Vasudevan, S. Jesse, Y. Kim, A. Kumar, S. V. Kalinin, *MRS Commun.* **2012**, *2*, 61.
[26] A. Roelofs, U. Bottger, R. Waser, F. Schlaphof, S. Trogisch, L. M. Eng, *Appl. Phys. Lett.* **2000**, *77*, 3444.
[27] Thin films, effective piezoelectric responses are typically measured. This is denoted by $d_{im,f}$ or $e_{im,f}$.
[28] K. Lefki, G. J. M. Dormans, *J. Appl. Phys.* **1994**, *76*, 1764.
[29] B. Y. Lee, J. Zhang, C. Zueger, W.-J. Chung, S. Y. Yoo, E. Wang, J. Meyer, R. Ramesh, S.-W. Lee, *Nat. Nanotechnol.* **2012**, *7*, 351.
[30] A. Kholkin, N. Amdursky, I. Bdikin, E. Gazit, G. Rosenman, *ACS Nano* **2010**, *4*, 610.
[31] C. Halperin, S. Mutchnik, A. Agronin, M. Molotskii, P. Urenski, M. Salai, G. Rosenman, *Nano Lett.* **2004**, *4*, 1253.
[32] S. V. Kalinin, S. Jesse, A. Tselev, A. P. Baddorf, N. Balke, *ACS Nano* **2011**, *5*, 5683.
[33] T. Jungk, A. Hoffmann, E. Soergel, *Appl. Phys. Lett.* **2006**, *89*, 163507.
[34] S. Jesse, A. Kumar, S. V. Kalinin, A. Gannepali, R. Proksch, *Microscopy Today* **2010**, *18*, 34.
[35] S. Jesse, S. V. Kalinin, R. Proksch, A. P. Baddorf, B. J. Rodriguez, *Nanotechnology* **2007**, *18*, 435503.
[36] B. J. Rodriguez, S. Jesse, A. P. Baddorf, S. V. Kalinin, *Phys. Rev. Lett.* **2006**, *96*, 237602.
[37] V. V. Shvartsman, A. L. Kholkin, *J. Appl. Phys.* **2007**, *101*, 064108.
[38] E. Soergel, *J. Phys. D: Appl. Phys.* **2011**, *44*, 464003.
[39] S. V. Kalinin, B. J. Rodriguez, S.-H. Kim, S.-K. Hong, A. Gruverman, E. A. Eliseev, *Appl. Phys. Lett.* **2008**, *92*, 152906.
[40] T. Jungk, A. Hoffmann, E. Soergel, *J. Appl. Phys.* **2007**, *102*, 084102.
[41] B. Rodriguez, A. Gruverman, A. Kingon, R. Nemanich, J. Cross, *J. Appl. Phys.* **2004**, *95*, 1958.
[42] A. Roelofs, N. A. Pertsev, R. Waser, F. Schlaphof, L. M. Eng, C. Ganpule, V. Nagarajan, R. Ramesh, *Appl. Phys. Lett.* **2002**, *80*, 1424.
[43] J. Y. Jo, S. M. Yang, T. H. Kim, H. N. Lee, J. G. Yoon, S. Park, Y. Jo, M. H. Jung, T. W. Noh, *Phys. Rev. Lett.* **2009**, *102*, 045701.
[44] A. Agronin, M. Molotskii, Y. Rosenwaks, G. Rosenman, B. J. Rodriguez, A. I. Kingon, A. Gruverman, *J. Appl. Phys.* **2006**, *99*, 104102.
[45] Y. Ishibashi, Y. Takagi, *J. Phys. Soc. Jpn.* **1971**, *31*, 506.
[46] M. Avrami, *J. Chem. Phys* **1940**, *8*, 212.
[47] A. K. Tagantsev, I. Stolichnov, N. Setter, J. S. Cross, M. Tsukada, *Phys. Rev. B* **2002**, *66*, 214109.
[48] D. J. Kim, J. Y. Jo, T. H. Kim, S. M. Yang, B. Chen, Y. S. Kim, T. W. Noh, *Appl. Phys. Lett.* **2007**, *91*, 132903.
[49] S. M. Yang, T. H. Kim, J.-G. Yoon, T. W. Noh, *Adv. Func. Mat.* **2012**, *22*, 2310.
[50] S. M. Yang, J. Y. Jo, T. H. Kim, J. G. Yoon, T. K. Song, H. N. Lee, Z. Marton, S. Park, Y. Jo, T. W. Noh, *Phys. Rev. B* **2010**, *82*, 174125.
[51] S. M. Yang, J.-G. Yoon, T. W. Noh, *Curr. Appl. Phys.* **2011**, *11*, 1111.
[52] T. Tybell, P. Paruch, T. Giamarchi, J.-M. Triscone, *Phys. Rev. Lett.* **2002**, *89*, 097601.
[53] G. Catalan, H. Bea, S. Fusil, M. Bibes, P. Paruch, A. Barthelemy, J. F. Scott, *Phys. Rev. Lett.* **2008**, *100*, 027602.
[54] S. Jesse, A. P. Baddorf, S. V. Kalinin, *Appl. Phys. Lett.* **2006**, *88*, 062908.
[55] S. Jesse, P. Maksymovych, S. V. Kalinin, *Appl. Phys. Lett.* **2008**, *93*, 112903.
[56] B. J. Rodriguez, S. Choudhary, Y. H. Chu, A. Bhattacharyya, S. Jesse, K. Seal, A. P. Baddorf, R. Ramesh, L.-Q. Chen, S. V. Kalinin, *Adv. Funct. Mater.* **2009**, *19*, 2053.
[57] B. J. Rodriguez, Y. H. Chu, R. Ramesh, S. V. Kalinin, *Appl. Phys. Lett.* **2008**, *93*, 142901.
[58] S. Jesse, B. J. Rodriguez, S. Choudhury, A. P. Baddorf, I. Vrejoiu, D. Hesse, M. Alexe, E. A. Eliseev, A. N. Morozovska, J. Zhang, L.-Q. Chen, S. V. Kalinin, *Nat. Mater.* **2008**, *7*, 209.
[59] V. R. Aravind, A. N. Morozovska, S. Bhattacharyya, D. Lee, S. Jesse, I. Grinberg, Y. L. Li, S. Choudhury, P. Wu, K. Seal, A. M. Rappe, S. V. Svechnikov, E. A. Eliseev, S. R. Phillpot, L. Q. Chen, V. Gopalan, S. V. Kalinin, *Phys. Rev. B* **2010**, *82*, 024111.
[60] N. Balke, S. Choudhury, S. Jesse, M. Huijben, Y. H. Chu, A. P. Baddorf, L. Q. Chen, R. Ramesh, S. V. Kalinin, *Nat. Nanotechnol* **2009**, *4*, 868.
[61] S. V. Kalinin, S. Jesse, B. J. Rodriguez, Y. H. Chu, R. Ramesh, E. A. Eliseev, A. N. Morozovska, *Phys. Rev. Lett.* **2008**, *100*, 155703.
[62] K. Seal, S. Jesse, M. Nikiforov, S. V. Kalinin, I. Fujii, P. Bintachitt, S. Trolier-McKinstry, *Phys. Rev. Lett.* **2009**, *103*, 57601.
[63] S. Jesse, H. N. Lee, S. V. Kalinin, *Rev. Sci. Instrum.* **2006**, *77*, 073702.
[64] J. P. Sethna, K. Dahmen, S. Kartha, J. A. Krumhansl, B. W. Roberts, J. D. Shore, *Phys. Rev. Lett.* **1993**, *70*, 3347.
[65] P. Bintachitt, S. Jesse, D. Damjanovic, Y. Han, I. M. Reaney, S. Trolier-McKinstry, S. V. Kalinin, *Proc. Nat. Acad. Sci. USA* **2010**, *107*, 7219.
[66] F. Griggio, S. Jesse, A. Kumar, D. M. Marincel, D. S. Tinberg, S. V. Kalinin, S. Trolier-McKinstry, *Appl. Phys. Lett.* **2011**, *98*, 212901.
[67] I. Fujii, E. Hong, S. Trolier-McKinstry, *IEEE Trans. Ultrason. Ferr.* **2010**, *57*, 1717.
[68] N. Pertsev, G. Arlt, *J. Appl. Phys.* **1993**, *74*, 4105.
[69] P. Bintachitt, S. Trolier-McKinstry, K. Seal, S. Jesse, S. V. Kalinin, *Appl. Phys. Lett.* **2009**, *94*, 042906.
[70] F. Griggio, S. Jesse, W. Qu, A. Kumar, O. Ovchinnikov, D. Tinberg, S. Kalinin, S. Trolier-McKinstry, *J. Appl. Phys.* **2011**, *110*, 044109.
[71] F. Griggio, S. Jesse, A. Kumar, O. Ovchinnikov, H. Kim, T. N. Jackson, D. Damjanovic, S. V. Kalinin, S. Trolier-McKinstry, *Phys. Rev. Lett.* **2012**, *108*, 157604.
[72] V. Nagarajan, A. Roytburd, A. Stanishevsky, S. Prasertchoung, T. Zhao, L. Chen, J. Melngailis, O. Auciello, R. Ramesh, *Nat. Mater.* **2003**, *2*, 43.

[73] S. Buhlman, B. Dwir, J. Baborowski, P. Muralt, *Appl. Phys. Lett* **2002**, *75*, 3195.

[74] S. S. N. Bharadwaja, S. Trolier-McKinstry, T. Mayer, P. Bettotti, L. Pavesi, *IEEE Trans. Ultrason. Ferr.* **2010**, *57*, 792.

[75] R. G. P. McQuaid, L. J. McGilly, P. Sharma, A. Gruverman, J. M. Gregg, *Nat. Commun.* **2011**, *2*, 404.

[76] C. S. Ganpule, V. Nagarajan, S. B. Ogale, A. L. Roytburd, E. D. Williams, R. Ramesh, *Appl. Phys. Lett.* **2000**, *77*, 3275.

[77] C. S. Ganpule, A. L. Roytburd, V. Nagarajan, B. K. Hill, S. B. Ogale, E. D. Williams, R. Ramesh, J. F. Scott, *Phys. Rev. B* **2001**, *65*, 014101.

[78] G. Arlt, U. Robels, *Integr. Ferroelectr.* **1993**, *3*, 343.

[79] B. E. Vugmeister, *Phys. Rev. B* **2006**, *73*, 174117.

[80] A. Kumar, F. Ciucci, A. N. Morozovska, S. V. Kalinin, S. Jesse, *Nat. Chem.* **2011**, *3*, 707.

[81] S. V. Kalinin, A. Kumar, N. Balke, M. McCorkle, S. Guo, T. Arruda, S. Jesse, *Adv. Mater. Processes* **2011**, *169*, 30.

[82] A. Kumar, Y. Ehara, A. Wada, H. Funakubo, F. Griggio, S. Trolier-McKinstry, S. Jesse, S. V. Kalinin, *J. Appl. Phys.* **2012**, *112*, 052021.

[83] Q. N. Chen, Y. Liu, Y. Liu, S. Xie, G. Cao, J. Li, *Appl. Phys. Lett.* **2012**, *101*, 063901.

[84] N. Balke, S. Jesse, Y. Kim, L. Adamczyk, A. Tselev, I. N. Ivanov, N. J. Dudney, S. V. Kalinin, *Nano Lett.* **2010**, *10*, 3420.

[85] N. Balke, S. Jesse, Y.-G. Kim, L. Adamczyk, I. N. Ivanov, N. J. Dudney, S. V. Kalinin, *ACS Nano* **2010**, *4*, 7349.

[86] S. V. Kalinin, N. Balke, *Adv. Mater.* **2010**, *22*, E193.

[87] A. Kumar, T. M. Arruda, Y. Kim, I. N. Ivanov, S. Jesse, C. W. Bark, N. C. Bristowe, E. Artacho, P. B. Littlewood, C.-B. Eom, S. V. Kalinin, *ACS Nano* **2012**, *6*, 3841.

[88] J. A. Sethian, *Level Set Methods and Fast Marching Methods: Evolving Interfaces in Computational Geometry, Fluid Mechanics, Computer Vision, and Materials Science*, Cambridge University Press, Cambridge UK **1999**.

[89] T. H. Kim, S. H. Baek, S. M. Yang, S. Y. Jang, D. Ortiz, T. K. Song, J. S. Chung, C. B. Eom, T. W. Noh, J. G. Yoon, *Appl. Phys. Lett.* **2009**, *95*, 262902.

[90] S. Yu, Y. Wu, R. Jeyasingh, D. Kuzum, H. Wong, *IEEE Trans. Electron Dev.* **2011**, *58*, 2729.

[91] S. H. Jo, T. Chang, I. Ebong, B. B. Bhadviya, P. Mazumder, W. Lu, *Nano Lett.* **2010**, *10*, 1297.

[92] S.-M. Yoon, S. Yang, S.-W. Jung, C.-W. Byun, M.-K. Ryu, W.-S. Cheong, B. Kim, H. Oh, S.-H. Ko Park, C.-S. Hwang, S.-Y. Kang, H.-J. Ryu, B.-G. Yu, *Appl. Phys. A* **2011**, *102*, 983.

[93] F. Preisach, *Z. Phys.* **1935**, *94*, 277.

[94] L. Néel, *Cah. Phys.* **1942**, *12*.

[95] H. Kronmüller, Z. Angew, *Physik* **1970**, *30*, 9.

[96] V. Mueller, Q. Zhang, *J. Appl. Phys.* **1998**, *83*, 3754.

[97] V. Mueller, Q. Zhang, *Appl. Phys. Lett.* **1998**, *72*, 2692.

[98] S. Jesse, S. V. Kalinin, *Nanotechnology* **2009**, *20*, 085714.

[99] I. T. Jolliffe, *Principal Component Analysis*, Springer, New York **2002**.

[100] Y. Kim, A. Kumar, O. Ovchinnikov, S. Jesse, H. Han, D. Pantel, I. Vrejoiu, W. Lee, D. Hesse, M. Alexe, S. V. Kalinin, *ACS Nano* **2012**, *6*, 491.

[101] R. E. Newnham, V. Sundar, R. Yimnirun, J. Su, Q. M. Zhang, *J. Phys. Chem. B* **1997**, *101*, 10141.

[102] A. Pramanick, D. Damjanovic, J. C. Nino, J. L. Jones, *J. Am. Cer. Soc.* **2009**, *92*, 2291.

[103] S. P. Leary, S. M. Pilgrim, *IEEE T. Ultrason. Ferr.* **1998**, *45*, 163.

[104] Y. Kim, A. Kumar, A. Tselev, I. I. Kravchenko, H. Han, I. Vrejoiu, W. Lee, D. Hesse, M. Alexe, S. V. Kalinin, S. Jesse, *ACS Nano* **2011**, *5*, 9104.

[105] K. Seeger, W. Maurer, *Solid State Commun.* **1978**, *27*, 603.

[106] N. Bassiri-Gharb, S. Trolier-McKinstry, D. Damjanovic, *J. Appl. Phys.* **2011**, *110*, 124104.

[107] N. B. Gharb, S. Trolier-McKinstry, D. Damjanovic, *J. Appl. Phys.* **2006**, *100*, 044107.

[108] S. Trolier-McKinstry, N. B. Gharb, D. Damjanovic, *Appl. Phys. Lett.* **2006**, *88*, 202901.

[109] S. V. Kalinin, A. N. Morozovska, L. Q. Chen, B. J. Rodriguez, *Rep. Prog. Phys.* **2010**, *73*, 056502.

[110] S. Kalinin, B. Rodriguez, S. Jesse, Y. Chu, T. Zhao, R. Ramesh, S. Choudhury, L. Chen, E. Eliseev, A. Morozovska, *Proc. Nat. Acad. Sci. USA* **2007**, *104*, 20204.

[111] A. N. Morozovska, E. A. Eliseev, S. V. Kalinin, *Appl. Phys. Lett.* **2006**, *89*, 192901.

[112] A. N. Morozovska, S. V. Svechnikov, E. A. Eliseev, B. J. Rodriguez, S. Jesse, S. V. Kalinin, *Phys. Rev. B* **2008**, *78*, 054101.

[113] M. Molotskii, *J. Appl. Phys.* **2003**, *93*, 6234.

[114] A. Kumar, O. Ovchinnikov, S. Guo, F. Griggio, S. Jesse, S. Trolier-McKinstry, S. V. Kalinin, *Phys. Rev. B* **2011**, *84*, 024203.

[115] O. S. Ovchinnikov, S. Jesse, P. Bintacchit, S. Trolier-McKinstry, S. V. Kalinin, *Phys. Rev. Lett.* **2009**, *103*, 157203.

[116] J. Sethna, *Statistical Mechanics: Entropy, Order Parameters and Complexity: Entropy, Order Parameters and Complexity*, Oxford University Press Oxford, New York **2006**.

[117] K. Binder, A. P. Young, *Rev. Mod. Phys.* **1986**, *58*, 801.

[118] K. Binder, *Rep. Prog. Phys.* **1997**, *60*, 487.

[119] Z. Chen, S. Haykin, J. J. Eggermont, S. Becker, *Correlative Learning: A Basis for Brain and Adaptive Systems*, Wiley, Hoboken **2007**.

[120] S. Haykin, *Neural Networks: A Comprehensive Foundation*, Prentice Hall, New York **1998**.

[121] T. M. Arruda, A. Kumar, S. V. Kalinin, S. Jesse, *Nano Lett.* **2011**, *11*, 4161.

[122] S. Guo, S. Jesse, S. Kalnaus, N. Balke, C. Daniel, S. V. Kalinin, *J. Electrochem. Soc.* **2011**, *158*, A982.

[123] S. Jesse, N. Balke, E. Eliseev, A. Tselev, N. J. Dudney, A. N. Morozovska, S. V. Kalinin, *ACS Nano* **2011**, *5*, 9682.

[124] S. V. Kalinin, A. Borisevich, D. Fong, *ACS Nano* **2012**, *6*, 10423.

[125] R. Waser, R. Dittmann, G. Staikov, K. Szot, *Adv. Mater.* **2009**, *21*, 2632.

[126] D. J. Kim, H. Lu, S. Ryu, C. W. Bark, C. B. Eom, E. Y. Tsymbal, A. Gruverman, *Nano Lett.* **2012**.